

Ngfr⁺ cholinergic projection from SI/nBM to mPFC selectively regulates temporal order recognition memory

Received: 10 September 2023

Accepted: 13 August 2024

Published online: 26 August 2024

 Check for updatesFan Mei¹, Chen Zhao², Shangjin Li², Zeping Xue^{3,4,5,6}, Yueyang Zhao^{3,4}, Yihua Xu², Rongrong Ye², He You², Peng Yu², Xinyu Han², Gregory V. Carr⁷, Daniel R. Weinberger⁷, Feng Yang^{3,4,6}✉ & Bai Lu^{2,4}✉

Acetylcholine regulates various cognitive functions through broad cholinergic innervation. However, specific cholinergic subpopulations, circuits and molecular mechanisms underlying recognition memory remain largely unknown. Here we show that *Ngfr*⁺ cholinergic neurons in the substantia innominate (SI)/nucleus basalis of Meynert (nBM)-medial prefrontal cortex (mPFC) circuit selectively underlies recency judgements. Loss of *nerve growth factor receptor* (*Ngfr*^{-/-} mice) reduced the excitability of cholinergic neurons in the SI/nBM-mPFC circuit but not in the medial septum (MS)-hippocampus pathway, and impaired temporal order memory but not novel object and object location recognition. Expression of *Ngfr* in *Ngfr*^{-/-} SI/nBM restored defected temporal order memory. Fiber photometry revealed that acetylcholine release in mPFC not only predicted object encounters but also mediated recency judgments of objects, and such acetylcholine release was absent in *Ngfr*^{-/-} mPFC. Chemogenetic and optogenetic inhibition of SI/nBM projection to mPFC in ChAT-Cre mice diminished mPFC acetylcholine release and deteriorated temporal order recognition. Impaired cholinergic activity led to a depolarizing shift of GABAergic inputs to mPFC pyramidal neurons, due to disturbed KCC2-mediated chloride gradients. Finally, potentiation of acetylcholine signaling upregulated KCC2 levels, restored GABAergic driving force and rescued temporal order recognition deficits in *Ngfr*^{-/-} mice. Thus, NGFR-dependent SI/nBM-mPFC cholinergic circuit underlies temporal order recognition memory.

Recognition memory refers to the ability to distinguish something novel from familiar. It involves the judgment of prior experiences on object, location, as well as their temporal order relationship^{1,2}. Experimentally, four subtypes of recognition memory tasks have been used in rats to examine the underlying mechanisms: novel object preference, temporal order, object location, and object-in-place^{2,3}. Lesions studies suggest that the perirhinal cortex (PRH) plays a key role in all four subtypes of recognition memory, whereas hippocampus

(HP) and medial prefrontal cortex (mPFC) are more involved in the spatial and temporal aspects of recognition rather than object recognition per se^{4,5}. Moreover, interference of acetylcholine (ACh)-releasing cholinergic projections to these critical brain structures also disturbs recognition memory. Cholinergic projection neurons predominantly reside in the basal forebrain (BF), and lesions of BF significantly damage recognition memory⁵⁻¹⁰. However, specific cholinergic circuits, namely cholinergic neurons from which BF nuclei

A full list of affiliations appears at the end of the paper. ✉ e-mail: fengyang@ccmu.edu.cn; bai_lu@tsinghua.edu.cn

projecting to which cortical or subcortical structures, underlie which subtypes and what aspects of recognition memory remain largely unknown. More importantly, how ACh signals help neuronal control of the spatial and temporal aspects of object recognition are not understood. By utilizing a newly developed ACh sensor capable of detecting ACh release with high sensitivity and spatiotemporal resolution during memory task, combined with chemogenetic and optogenetic technologies to manipulate the activity of cholinergic neurons, we may uncover the intricate relationship between ACh dynamics and the precise behavioral outcomes associated with recognition memory^{11,12}.

In addition to BF, the cholinergic neurons are dispersed in many brain regions including the brainstem, thalamus, striatum, and cortex, and regulate a wide variety of physiological functions ranging from sleep, attention, to mood and memory^{11,13}. An important task in modern neuroscience is to determine the functional heterogeneity of the cholinergic neurons and their molecular signature within each anatomical boundary. Within BF, the cholinergic projection neurons are clustered in a series of nuclei following a rostral to caudal direction, including the medial septum (MS), the vertical and horizontal subdivisions of the diagonal band (vDB, hDB), the ventral pallidum (VP), the substantia innominate (SI) and the nucleus basalis of Meynert (nBM). During the development, the caudally located cholinergic neurons are early-born (SI/nBM), whereas the rostrally located cholinergic neurons are later-born (MS/DB), under different transcriptional controls¹⁴. In addition to the subcluster segregation by birthdate, the BF cholinergic projection neurons are specified by their outputs and function. Specifically, the MS, VP, and DB cholinergic neurons form functional clusters that project primarily to the hippocampus, parahippocampus, olfactory bulb, and midline cortical structures. By contrast, the SI and nBM subpopulations predominantly innervate the neocortex and amygdala¹⁵. While the BF cholinergic subpopulations show broad heterogeneity, the functional significance underlying the diverse cholinergic subpopulations remains elusive.

Differentiation of BF cholinergic neurons is supported by the neurotrophic factors derived from projection targets¹⁶. Accordingly, cholinergic neurons express neurotrophic receptors for signaling transduction, including NGFR (also known as p75^{NTR}), TRKA, TRKB, and TRKC¹¹. Among these, NGFR shows remarkable changes in expression pattern along brain development. At the embryonic stage, NGFR is expressed in many types of neurons but its expression dramatically declines postnatally¹⁷. Cell culture experiments demonstrated that activation of NGFR by proBDNF, the precursor of brain-derived neurotrophic factor (BDNF), could lead to axonal collapses, dendritic atrophy, and spine shrinkage^{17–20}. It appears that the proper development of the nervous system requires a balance between proBDNF-NGFR and mature BDNF-TrkB signaling^{17,20}. In the adult brain, NGFR is robustly and almost exclusively expressed in BF cholinergic neurons^{21–23}. Whether NGFR regulates the survival and/or function of BF cholinergic neurons remains unresolved. Both increase and decrease in the number of BF cholinergic neurons were reported using various *Ngfr* knockout mice^{24–32}. The apparent effect of NGFR on cell death seems inconsistent with its selectively high expression in BF cholinergic neurons in the adult brain, suggesting that the major function for NGFR may not be for the survival of these neurons.

What is the molecular and circuitry mechanism underlying the integrated cholinergic regulation of recognition memory? In this study, we illustrate the functional specificity of *Ngfr*⁺ cholinergic projection neurons and examine their selective regulation of three types of recognition. Using single-cell RNA sequencing data, we characterized the molecular signature of cholinergic subpopulations from different anatomical boundaries. Chemogenetic and optogenetic manipulation of cholinergic circuitry was performed to determine the differential effect of cholinergic innervations in recency judgments. To understand how ACh signals help to discriminate objects in temporal order, we monitored ACh dynamics with an advanced high sensitivity

ACh sensor, coupled with detailed behavioral changes during the recognition process. Further, a series of electrophysiological recordings were performed to unravel the effect of cholinergic activity in shaping GABAergic transmission polarity, which mediates recency judgments. Collectively, our results suggest that *Ngfr*⁺ SI/nBM-mPFC circuit selectively regulates recency judgment in recognition memory.

Results

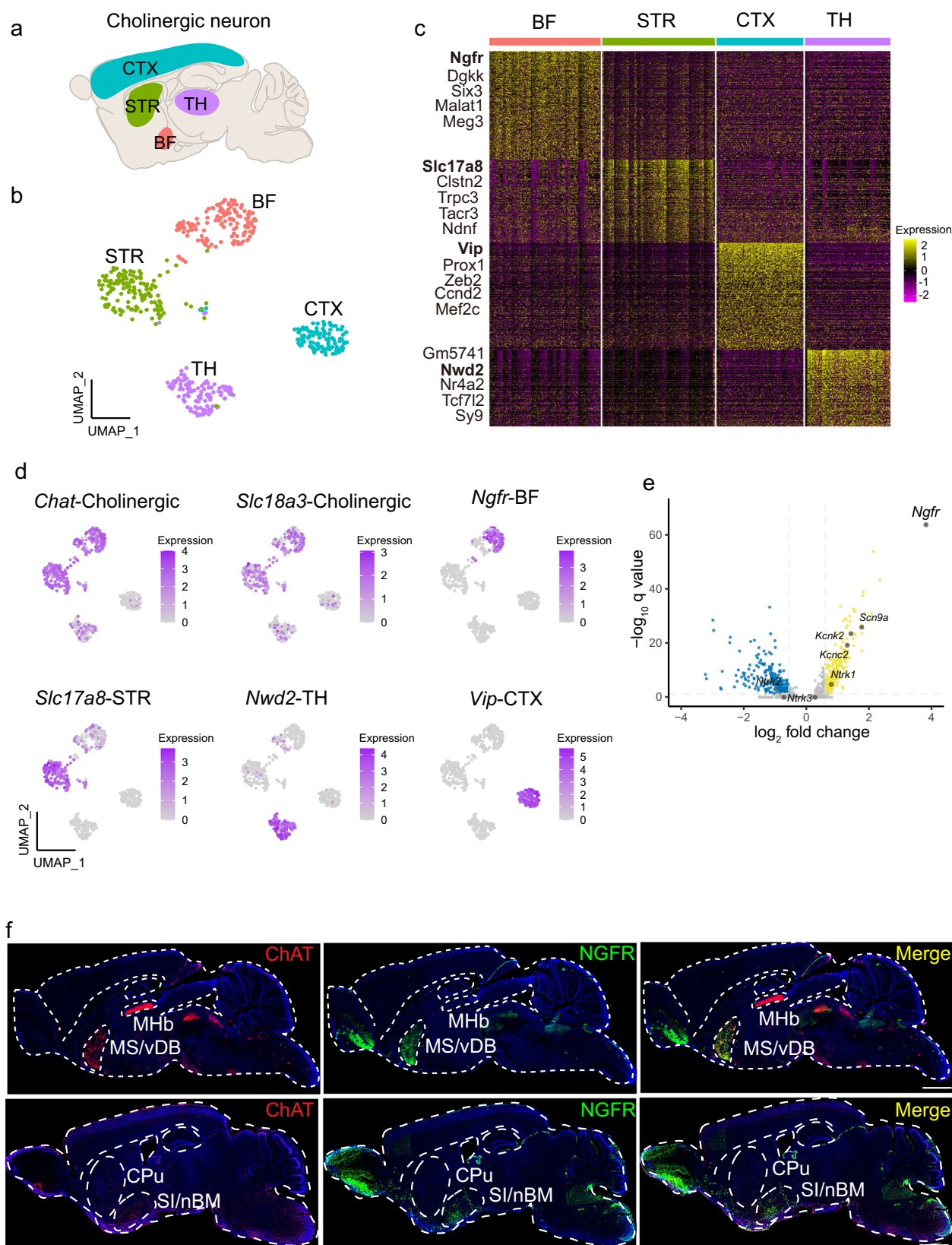
Ngfr specifies cholinergic projection neurons in BF

Previous studies have classified four types of cholinergic neurons, based on their anatomical locations: (1) projection neurons in the BF and brainstem; (2) interneurons in the striatum, cortex, and hippocampus; (3) glutamatergic neurons in the thalamus, and (4) motor neurons in the hindbrain and spinal cord^{11,13,33}. We employed the single-cell RNA sequencing datasets, which established an atlas of cell-type-specific gene expression patterns of the adolescent and adult mouse nervous system, to investigate the molecular signatures of different types of cholinergic neurons. In the DropViz single-cell RNA sequencing dataset³⁴, we analyzed cholinergic neurons distributed in different brain regions, including globus pallidus externus and nucleus basalis (66,318 cells), thalamus (89,027 cells), frontal cortex (156,167 cells), posterior cortex (99,186 cells), and striatum (77,037 cells) (Fig. 1a). Cholinergic neurons are defined by the specific expression of choline acetyltransferase (CHAT, encoded by *Chat*) and the vesicular ACh transporter (VACHT, encoded by *Slc18a3*). Cholinergic neurons from these anatomical boundaries were integrated into a uniform manifold approximation and projection (UMAP) space (Fig. 1b). Interestingly, cholinergic neurons from different anatomical locations showed remarkable molecular diversity (Fig. 1c). To define the molecular signature for each cholinergic cluster, top differentially expressed genes (DEGs) were selected for further analysis. Subclustering analysis identified *Ngfr* as a key marker for cholinergic neurons originating from the BF, while *Slc17a8* for those from the striatum. *Nwd2* labels the cholinergic population originating from the thalamus, and *Vip* marks the subpopulation of cholinergic neurons in the cortex (Fig. 1d). To corroborate these findings, we examined these molecular markers using another single-cell RNA sequencing dataset Mousebrain³⁵. *Chat*-expressing cholinergic neurons from different anatomical locations were clustered by UMAP (Supplementary Fig. 1a). Consistently, *Ngfr* exclusively marked BF cholinergic neuron (cluster: DECHO1). Likewise, *Slc17a8* labeled cholinergic subcluster in the striatum (cluster: TECHO), *Nwd2* tagged neurons originating from the thalamus (cluster: DECHO2), and *Vip* marked those from the cortex (cluster: TEINH4), respectively (Supplementary Fig. 1b). Thus, molecular markers for each cholinergic subcluster are strongly correlated between individual datasets.

Moreover, comparison of the expression pattern of BF cholinergic neurons and that from the other three regions in the DropViz and Mousebrain dataset, we found that *Ngfr*, rather than the other reported neurotrophic receptors, showed exclusively abundant expression in the BF (Fig. 1e and Supplementary Fig. 1c–e). To validate these results, we performed immunofluorescence of cholinergic neurons in the brain of adult mice. Cholinergic neurons labeled with ChAT were identified in the MS/vDB and SI/nBM within BF, habenula within the thalamus, and caudate putamen within the striatum (Fig. 1f). By contrast, we only detected NGFR expression in the ChAT⁺ cholinergic neurons from BF, but not those from habenula or caudate putamen. Therefore, our findings provide solid evidence that *Ngfr* serves as a defining marker for BF cholinergic projection neurons.

NGFR regulates the excitability of cholinergic neuron in SI/nBM but not MS

We further analyzed the enriched biological processes associated with distinct expression patterns of the *Ngfr*⁺ cholinergic neurons in the BF versus *Ngfr* cholinergic neurons in the other anatomical locations.



Based upon the DropViz and Mousebrain single-cell RNA sequencing datasets, GSEA analyses using GO annotation indicated that pathways related to the regulation of synaptic signaling, neurotransmitter transport, exocytosis and vesicle-mediated transport in synapse are associated with NGFR expression (Fig. 2a and Supplementary Fig. 2a). These results suggest that NGFR may regulate cholinergic neuronal

activity and synaptic transmission. Thus, we investigated whether disruption of *Ngfr* would affect the excitability of cholinergic neuron. To this end, *Ngfr*^{+/+} and *Ngfr*^{-/-} mice were crossed with a ChAT-EGFP transgenic line so that all BF cholinergic neurons were labeled with green fluorescence protein (GFP) (Supplementary Fig. 2b). Previous studies demonstrated that SI/nBM and MS cholinergic neurons, the

Fig. 1 | *Ngfr* specifies cholinergic projection neurons in BF. **a** Schematic illustration of the cholinergic neurons that dispersed in the basal forebrain (BF), striatum (STR), cortex (CTX), and thalamus (TH). **b** Visualization of cholinergic neuron clusters from different anatomic boundaries using UMAP (single-cell RNA sequencing data from the DropViz dataset). Numbers of *Chat*⁺ cholinergic neuron sampled in each region are indicated. BF, $n = 142$ cells; STR, $n = 144$ cells; CTX, $n = 111$ cells; TH, $n = 109$ cells. **c** Hierarchical clustering of the expression profile of cholinergic neurons from different regions. Top five differentially expressed genes (DEGs) in each cholinergic cluster are indicated. **d** Visualization of each cholinergic cluster using specific marker genes in UMAP. Cholinergic, *Chat* and *Slc18a3*; basal forebrain, *Ngfr*; striatum, *Slc17a8*; thalamus, *Nwd2*; cortex, *Vip*. **e** Volcano plot

showing the DEGs that differentiate the BF cholinergic projection neurons from the other cholinergic clusters. Top DEGs are highlighted (\log_2 fold change > 1 , $q < 0.05$). \log_2 fold change > 1 indicates genes enriched in the BF cholinergic neurons. **f** Spatial distribution of ChAT and NGFR expression. Sagittal brain section of wild-type mice at the age of 3 months is subjected to immunofluorescence staining. NGFR co-localized with ChAT⁺ cholinergic neurons in the MS/vDB (top row) and SI/nBM (bottom row), but not with the cholinergic neurons in the MHB (top row) and CPU (bottom row). MHB medial habenular nucleus, CPU caudate putamen. Scale bar, 1 mm. Statistical analyses in (c) and (e) were performed by two-sided Wilcoxon rank-sum test, p value adjusted by false discovery rate (FDR) to get the q value.

two subpopulations of BF cholinergic neurons, exhibit distinct features in fate specification, spatial localization and projecting patterns¹¹. Specifically, the caudally located early-born SI/nBM cholinergic neurons project primarily to mPFC and other cortical regions, whereas rostrally located late-born MS cholinergic neurons mainly innervate hippocampus and subcortical structures. Thus, we performed whole-cell clamp recordings of these two subpopulations separately. A depolarizing current step triggered a train of action potentials in the cholinergic neurons of the SI/nBM from the *Ngfr*^{+/+} mice. Surprisingly, the identical depolarizing current step resulted in a significantly reduced number of action potentials in the *Ngfr*^{-/-} SI/nBM cholinergic neuron (Fig. 2b). A systematic analysis using depolarizing steps of increasing amplitudes demonstrated a consistent decrease in the firing frequency of *Ngfr*^{-/-} neurons as compared with the *Ngfr*^{+/+} neurons, suggesting a reduced excitability in the SI/nBM neurons of the *Ngfr*^{-/-} mice (Fig. 2c). Next, whole-cell current-clamp recordings were performed on the MS cholinergic neurons (Fig. 2d). Interestingly, spike frequency was not altered in the *Ngfr*^{-/-} MS cholinergic neurons (Fig. 2e). Further, we examined the membrane electrophysiological properties (resting membrane potential (RMP), input resistance, action potential threshold, amplitude and half-width) of SI/nBM and MS cholinergic neurons, and found no difference between *Ngfr*^{+/+} and *Ngfr*^{-/-} mice (Supplementary Table 1). These data indicate that NGFR selectively regulates the excitability of a subpopulation of BF cholinergic neurons in the SI/nBM, but not those in the MS.

To determine whether the changes in neuronal excitability are due to an alteration of health and wellbeing of the SI/nBM neurons, we examined the cholinergic cell number from the SI/nBM in the *Ngfr*^{-/-} mice. Quantification of ChAT⁺ cell number in the SI/nBM indicated no significant difference between *Ngfr*^{+/+} and *Ngfr*^{-/-} mice (Supplementary Fig. 2c, d, *Ngfr*^{+/+}, 40.43 ± 1.15 ; *Ngfr*^{-/-}, 43.76 ± 1.93). We thus demonstrated that NGFR regulates cholinergic activity without affecting cholinergic cell number at the adult stage of *Ngfr*^{-/-} mice.

Ngfr^{-/-} mice show defective temporal order recognition memory

Next, we investigated the behavioral outcome of changes in the SI/nBM neuron excitability. It has been reported that IgG 192 saporin lesions of cholinergic inputs from BF lead to recognition memory deficits³⁶. Given NGFR's differential regulation of BF cholinergic subpopulations, we investigated three specific types of recognition memory. These types correspond to temporal order, novel object, and object location recognition², which represent the ability to discern recency, familiarity, and location, respectively³. The object-in-place test was too difficult for mice to perform and therefore was not examined. In the temporal order recognition test, mice were exposed to two identical objects in sample phase 1 and 1 h later to another two identical objects (but different from those used in sample phase 1) in sample phase 2. After 3 h, mice would generally spend more time exploring the object from sample phase 1, compared to that from sample phase 2, owing to instinctive tendency to explore the earlier acquaintance of the two familiar objects (Fig. 3a). We found that unlike the *Ngfr*^{+/+} mice, the *Ngfr*^{-/-} mice did not show a preference for the

earlier objects from sample phase 1. The discrimination ratio in the test phase was 0.54 ± 0.09 for *Ngfr*^{+/+} mice and 0.01 ± 0.08 for *Ngfr*^{-/-} mice (Fig. 3b). These results suggest that loss of NGFR leads to significant impairment in temporal order recognition memory. There was no difference between *Ngfr*^{+/+} and *Ngfr*^{-/-} mice in the total time spent exploring the objects during sample phase 1, sample phase 2, and test phase (Fig. 3c). Moreover, *Ngfr*^{+/+} and *Ngfr*^{-/-} mice exhibited similar overall locomotor activity (Fig. 3d, e). Thus, the reduction in discrimination ratio in the temporal order recognition test seen in *Ngfr*^{-/-} mice was not due to deficits in motor control. Taken together, we found that *Ngfr*, as a unique molecular identifier of BF cholinergic neurons, regulates behavioral outputs of temporal order recognition memory.

To determine whether the familiarity and spatial aspects of recognition memory were affected in *Ngfr*^{-/-} mice, we further performed novel object recognition and object location preference tests. In the novel object recognition test, mice were initially exposed to two identical objects during the sample phase, followed by a test phase where they were presented with one familiar object and one novel object (Fig. 3f). Mice generally spent more time on the novel object as compared with the familiar one. In this test, *Ngfr*^{+/+} and *Ngfr*^{-/-} mice exhibited no statistical difference in discrimination ratio (Fig. 3g, *Ngfr*^{+/+}, 0.48 ± 0.12 ; *Ngfr*^{-/-}, 0.31 ± 0.09). In the object location preference test, mice were initially exposed to two identical objects during the sample phase. After 1 h interval, the mice were presented with the same two objects again, with one object in its original location and the other in a new location (Fig. 3i). Mice likely spent more time on the object relocated to a new location. Again, the *Ngfr*^{+/+} and *Ngfr*^{-/-} mice showed no significant difference in the object location recognition (Fig. 3j, *Ngfr*^{+/+}, 0.42 ± 0.13 ; *Ngfr*^{-/-}, 0.30 ± 0.11). There was no statistical difference between *Ngfr*^{+/+} and *Ngfr*^{-/-} mice in the amount of time spent exploring the objects during the sample phase and test phase in each of these two tests (Fig. 3h, k). These results indicate that NGFR specifically regulates recency judgment but not familiarity discrimination or spatial recognition.

To determine whether impairment in temporal order recognition in *Ngfr*^{-/-} mice was attributable to development compensatory effects, we performed both rescue experiments in adult *Ngfr*^{-/-} mice and cholinergic-specific knockdown of *Ngfr* expression experiments in adult wild-type mice. Specifically, we bilaterally injected *Ngfr*-expressing adeno-associated virus (AAV) 9 or control virus under the control of cholinergic-specific promoter into SI/nBM of *Ngfr*^{-/-} mice at ages of 2–5 months. Immunofluorescence staining revealed significant NGFR immunoreactivity in SI/nBM but not in other regions, indicating re-expression of NGFR in the *Ngfr*^{-/-} mice (Supplementary Fig. 3a, bottom row). Behavioral tests were performed 4 weeks after *Ngfr*-virus injection. We found that NGFR expression in SI/nBM rescued the impairment in temporal order recognition memory (Supplementary Fig. 3b, *Ngfr*^{-/-}:control, -0.23 ± 0.15 ; *Ngfr*^{-/-}:*Ngfr*, 0.15 ± 0.07), without affecting novel object recognition (Supplementary Fig. 3c, *Ngfr*^{-/-}:control, 0.06 ± 0.05 ; *Ngfr*^{-/-}:*Ngfr*, 0.14 ± 0.04) and object location recognition (Supplementary Fig. 3d, *Ngfr*^{-/-}:control, 0.17 ± 0.06 ; *Ngfr*^{-/-}:*Ngfr*, 0.13 ± 0.07). Moreover, we bilaterally injected AAV9-ChAT-mini

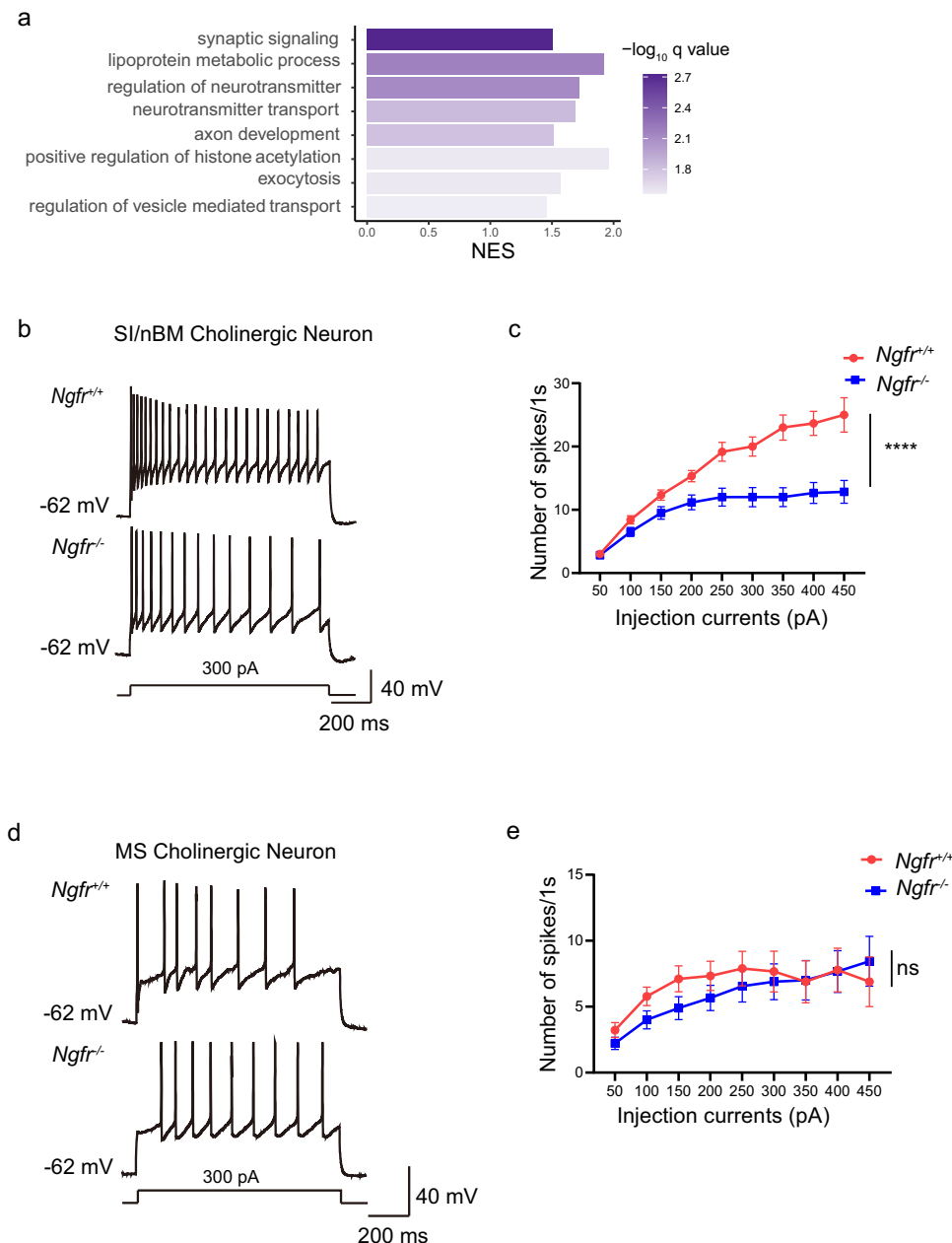
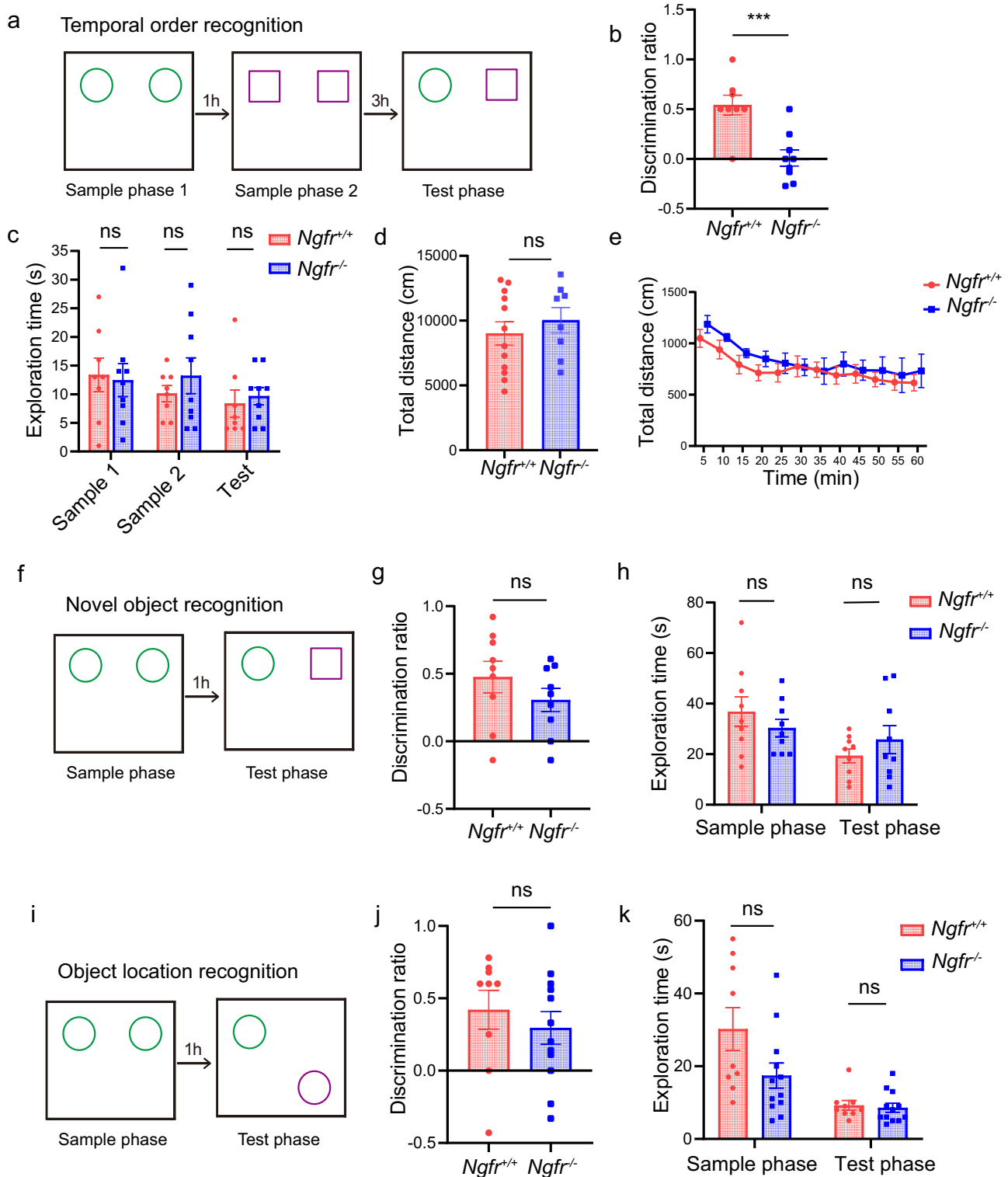


Fig. 2 | *Ngfr*^{-/-} mice show decreased intrinsic excitability of cholinergic neurons in SI/nBM but not MS. **a** Gene set enrichment analysis (GSEA) of gene expression profiles of BF cholinergic projection neurons versus cholinergic clusters from the other brain regions (single-cell RNA sequencing data from the DropViz dataset). The GO database is used for the annotation of biological process. GSEA results are plotted based on the normalized enrichment scores (NES). q values for each pathway are determined by FDR. **b** Representative traces of cholinergic action potential discharges evoked by long depolarization pulse (300 pA, 1 s) in the SI/nBM of both *Ngfr*^{+/+} and *Ngfr*^{-/-} mice. **c** Intrinsic excitability is calculated as action potential numbers plotted against the depolarizing currents injected into the cholinergic neuron in whole-cell current-clamp recordings. The excitability of SI/

nBM cholinergic neurons of *Ngfr*^{-/-} mice was significantly lower than that of *Ngfr*^{+/+} mice. $F_{\text{interaction}}(8,176) = 10.24, p < 0.0001$; $F_{\text{currents}}(1.40,30.74) = 61.41, p < 0.0001$; $F_{\text{genotype}}(1,22) = 17.21, p = 0.0004$. *Ngfr*^{+/+}, $n = 12$ cells from 7 mice; *Ngfr*^{-/-}, $n = 12$ cells from 7 mice. **d** Representative traces of cholinergic action potentials evoked by long depolarization pulse (300 pA, 1 s) in the MS. **e** Quantification plots of MS cholinergic neuron action potential numbers against a series of depolarizing events. $F_{\text{interaction}}(8,128) = 1.21, p = 0.30$; $F_{\text{currents}}(1.51,24.11) = 9.32, p = 0.0022$; $F_{\text{genotype}}(1,16) = 0.28, p = 0.61$. *Ngfr*^{+/+}, $n = 9$ cells from 5 mice; *Ngfr*^{-/-}, $n = 9$ cells from 7 mice. Numerical data are means \pm SEM. Statistical analyses in (c) and (e) were performed by two-way ANOVA with Sidak's multiple comparisons. **** $p < 0.0001$; ns not significant. Source data are provided as a Source Data file.

TK promoter-miR30shRNA(*Ngfr*), which would knockdown *Ngfr* expression through antisense shRNA, or the control virus, into SI/nBM of wild-type mice at ages of 2–3 months. Immunofluorescence staining revealed a marked reduction in NGFR expression in the wild-type SI/nBM cholinergic neurons (Supplementary Fig. 3e, bottom row). Consistently, reduction in NGFR expression significantly deteriorated temporal order recognition (Supplementary Fig. 3f, *Control*, 0.32 ± 0.10 ; *Ngfr shRNA*, -0.37 ± 0.10), leaving intact the

novel object recognition (Supplementary Fig. 3g, *Control*, 0.17 ± 0.06 ; *Ngfr shRNA*, 0.05 ± 0.05) and the object location recognition (Supplementary Fig. 3h, *Control*, 0.26 ± 0.07 ; *Ngfr shRNA*, 0.14 ± 0.04). Taken together, these data provided solid evidence that the SI/nBM *Ngfr* expression controls temporal order recognition by regulating the electrophysiological function of the cholinergic neurons itself in the adult, rather than affecting nervous system development in general.



Decreased ACh release in mPFC underlies defective temporal order recognition in $Ngfr^{-/-}$ mice

The cholinergic neurons in the SI/nBM project to cortical regions, and among them, mPFC has been reported as a main cholinergic target for the complex temporal order recognition process^{3,37,38}. We therefore examined ACh release in mPFC using a newly developed ACh fluorescent indicator ACh3.0, and examined ACh dynamics in mice performing temporal order recognition memory task. The improved ACh3.0 sensor exhibits precise spatiotemporal resolution in ACh detection^{39,40}. The ACh3.0 sensor delivered by the AAV system

together with the optical fiber was introduced to the mPFC of $Ngfr^{+/+}$ and $Ngfr^{-/-}$ mice (Fig. 4a). Strong GFP signal indicated expression of ACh3.0 sensor (Fig. 4b). The fluorescent signal representing ACh release in mPFC was recorded by photometry, and the correlation between ACh dynamics and behavioral outcomes was analyzed. Remarkably, we found that the rising of ACh signal always occurred 1-2 s before wild-type mice encountered the objects, and declined rapidly when they moved away from the exploration of objects, suggesting that the ACh signal may function as an initiator for the recognition processing (Fig. 4c, d and Supplementary Movie 1).

Fig. 3 | *Ngfr*^{-/-} mice show defective temporal order recognition memory.

a Diagram of temporal order recognition test. **b** Performance of temporal order memory is assessed by discrimination ratio in the test phase, as defined as “(exploration time of the object from sample phase 1 – exploration time of the object from sample phase 2)/total exploration time”. *Ngfr*^{-/-} mice exhibited a significantly decreased discrimination ratio in temporal order recognition compared with *Ngfr*^{+/+} mice. $p = 0.0008$. The number of mice used in this and all other figures is indicated by n . *Ngfr*^{+/+}, $n = 8$; *Ngfr*^{-/-}, $n = 9$. **c** No significant difference in the exploration time during each sample and test phase of the temporal order recognition test between genotypes. *Ngfr*^{+/+}, $n = 8$; *Ngfr*^{-/-}, $n = 9$. **d, e** No significant difference in locomotor activity in *Ngfr*^{+/+} and *Ngfr*^{-/-} mice. Total distance, $p = 0.48$ (**d**) and distance traveled per 5-min intervals (**e**) are analyzed. $F_{\text{interaction}}(11,198) = 0.42$, $p = 0.95$; $F_{\text{time}}(3.74,67.38) = 11.52$, $p < 0.0001$; $F_{\text{genotype}}(1,18) = 0.52$, $p = 0.48$. *Ngfr*^{+/+}, $n = 12$; *Ngfr*^{-/-}, $n = 8$. **f** Diagram of novel object recognition memory test. **g** For the novel object recognition, the discrimination ratio represented the time spent

exploring the novel object minus the time spent exploring the familiar object divided by the total exploration time. *Ngfr*^{+/+}, $n = 9$; *Ngfr*^{-/-}, $n = 9$. **h** No significant difference in the exploration time between genotypes during the sample and test phase of novel object recognition. *Ngfr*^{+/+}, $n = 9$; *Ngfr*^{-/-}, $n = 9$. **i** Diagram of object location recognition memory test. **j** For the object location recognition, the discrimination ratio represented the time spent exploring the displaced object minus time spent exploring the object in the familiar location divided by the total exploration time. *Ngfr*^{+/+}, $n = 9$; *Ngfr*^{-/-}, $n = 12$. **k** No significant difference between genotypes in the exploration time during the sample and test phase of the object location recognition test. *Ngfr*^{+/+}, $n = 9$; *Ngfr*^{-/-}, $n = 12$. Numerical data are means \pm SEM. Statistical analyses were performed by unpaired two-sided t -test in (**b**), (**d**), (**g**), and (**j**), and two-way ANOVA with Bonferroni’s multiple comparisons in (**c**), (**e**), (**h**), and (**k**). *** $p < 0.001$; ns not significant. Source data are provided as a Source Data file.

Moreover, we determined whether ACh release is involved in object discrimination and recency judgments in the wild-type mice. There was a rise in ACh release during object encounter, but no significant difference in ACh levels when the mice explored the two identical objects, either in the sample phase 1 (left object, 0.57 ± 0.06 ; right object, 0.52 ± 0.05) or sample phase 2 (left object, 0.50 ± 0.05 ; right object, 0.50 ± 0.05). Interestingly, in the test phase, ACh signals were significantly higher when the mice explored the earlier object from sample phase 1 than that when they explored the later object from sample phase 2 (Fig. 4e, earlier object, 0.67 ± 0.09 ; later object, 0.32 ± 0.08). Taken together, these data support the notion that the rise in ACh signals not only predicts object encounters, but also plays a crucial role in discriminating earlier versus later objects.

By contrast, the photometry recording for the sample phases and test phase revealed almost no surge of ACh transients in the *Ngfr*^{-/-} mice (Fig. 4c, d). Group summary of the peak ACh signals during object encounters in the recognition processing indicated a significantly decreased fluorescence response in *Ngfr*^{-/-} mice (Fig. 4f, sample phase 1, *Ngfr*^{+/+}, 0.63 ± 0.09 ; *Ngfr*^{-/-}, 0.18 ± 0.04 ; sample phase 2, *Ngfr*^{+/+}, 0.73 ± 0.13 ; *Ngfr*^{-/-}, 0.21 ± 0.07 ; test phase, *Ngfr*^{+/+}, 0.76 ± 0.10 ; *Ngfr*^{-/-}, 0.14 ± 0.06). These findings offer compelling evidence that NGFR is required for ACh release from cholinergic afferents in mPFC, and disruption of NGFR impairs recency judgment in recognition by reducing ACh release in mPFC.

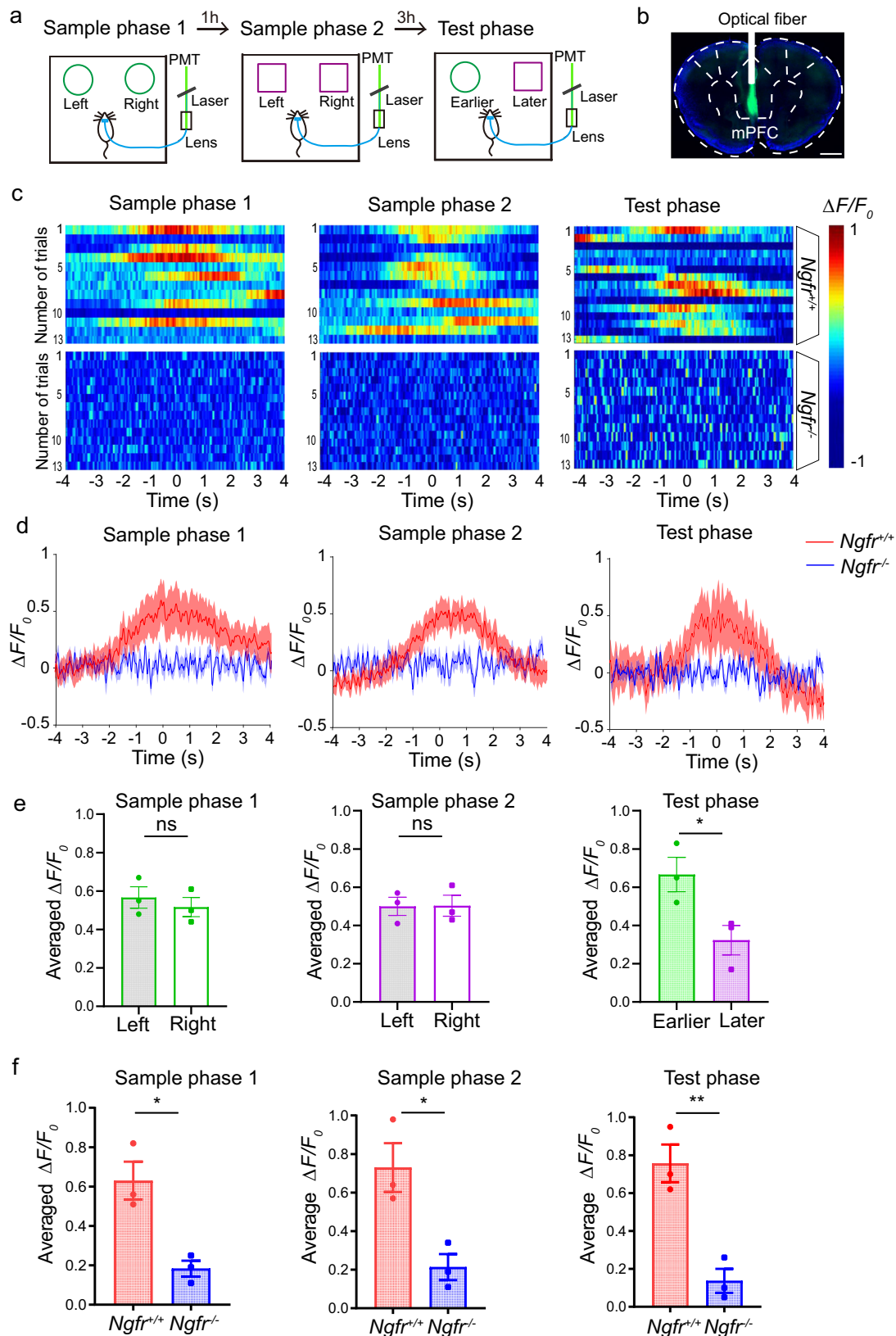
Next, we systematically examined mPFC ACh dynamics in the other two types of recognition memory. In novel object recognition test (Supplementary Fig. 4a), ACh release in mPFC only occurred in the sample phase in *Ngfr*^{+/+} mice but not *Ngfr*^{-/-} mice (Supplementary Fig. 4b–d, left, *Ngfr*^{+/+}, 0.55 ± 0.11 ; *Ngfr*^{-/-}, 0.12 ± 0.03), and no ACh signals were detected in the test phase (Supplementary Fig. 4b–d, right, *Ngfr*^{+/+}, 0.08 ± 0.02 ; *Ngfr*^{-/-}, 0.07 ± 0.02). Likewise, in object location recognition (Supplementary Fig. 4e), the rise of ACh was seen only in the sample phase (Supplementary Fig. 4f–h, left, *Ngfr*^{+/+}, 0.50 ± 0.11 ; *Ngfr*^{-/-}, 0.08 ± 0.01), but not in the test phase (Supplementary Fig. 4f–h, right, *Ngfr*^{+/+}, 0.09 ± 0.02 ; *Ngfr*^{-/-}, 0.11 ± 0.02). Thus, although ACh release in mPFC in the sample phase appears to be associated with object encounter, it is not required for recognition of novel object or its specific location. The lack of mPFC ACh signals in the test phase either in *Ngfr*^{+/+} or *Ngfr*^{-/-} mice further supports the notion that SI/nBM-mPFC cholinergic circuit is not involved in the novel object or object location recognition.

Inhibition of ACh release in the SI/nBM-mPFC circuit impairs temporal order recognition

To determine whether the SI/nBM-mPFC cholinergic projection is essential for temporal order recognition memory, we interfered this specific circuit in ChAT-Cre mice using chemogenetic hM4D(Gi) delivered through AAV-Retro virus retrograde labeling system. Cre-dependent hM4D(Gi)-mCherry AAV-Retro virus or the control virus

was bilaterally injected into the mPFC of ChAT-Cre mice, which would retrogradely transport from mPFC to SI/nBM and specifically inhibit the ChAT-expressing SI/nBM cholinergic neurons (Fig. 5a). Immunofluorescence suggested hM4D expression in the SI/nBM cholinergic neurons (Supplementary Fig. 5a). We performed temporal order recognition test 1 h after intraperitoneal injection of Clozapine N-oxide (CNO), which binds hM4D to inhibit the cholinergic activities in SI/nBM. As expected, selective inhibition of SI/nBM-mPFC circuit significantly deteriorated temporal order memory, as compared with the control group (Fig. 5b, mCherry, 0.30 ± 0.09 ; hM4D, -0.06 ± 0.06). Comparatively, novel object recognition was not affected by the selective inhibition of SI/nBM-mPFC circuit (Supplementary Fig. 5b, test phase, mCherry, 0.43 ± 0.11 ; hM4D, 0.42 ± 0.05). These data are consistent with previous studies showing that lesions in mPFC impair temporal order recognition but not novel object recognition². Moreover, we examined whether the other cholinergic subpopulation, MS/vDB, is involved in temporal order recognition. AAV carrying hM4D was injected into the MS/vDB of ChAT-Cre mice to achieve specific inactivation of the cholinergic subpopulation (Supplementary Fig. 5c). Chemogenetic inhibition of the MS/vDB cholinergic neurons did not affect temporal order recognition (Supplementary Fig. 5d, test phase, mCherry, 0.27 ± 0.10 ; hM4D, 0.15 ± 0.15). Taken together, these data demonstrate the specific role of SI/nBM-mPFC cholinergic circuit in the selective regulation of temporal order recognition.

In addition, we recorded ACh dynamics during the temporal order recognition test (Fig. 5c). Fiber photometry recording revealed rising ACh signals during object encounters in ChAT-Cre mice with control virus. By contrast, a significant reduction in ACh release was observed in the ChAT-Cre mice injected with hM4D virus (Fig. 5d). Statistical quantification revealed that inhibition of SI/nBM cholinergic neuron impaired ACh release in mPFC in both the sample phases and test phase (Fig. 5e, sample phase 1, mCherry, 0.69 ± 0.08 ; hM4D, 0.38 ± 0.05 ; sample phase 2, mCherry, 0.63 ± 0.10 ; hM4D, 0.23 ± 0.04 ; test phase, mCherry, 0.73 ± 0.11 ; hM4D, 0.27 ± 0.08). Thus, these data demonstrate that cholinergic activity in the SI/nBM-mPFC circuit plays a critical role in determining temporal order recognition memory. Next, we inactivated mPFC-projecting cholinergic neurons by optogenetic manipulations. AAV carrying eNpHR3.0-mCherry was injected into the SI/nBM area of the ChAT-Cre mice bilaterally (Fig. 5f). As shown in Supplementary Fig. 5e, immunofluorescence indicated halorhodopsin expression specifically in ChAT-expressing SI/nBM cholinergic neurons. Meanwhile, eNpHR3.0-mCherry-expressing terminals were observed in mPFC, reflecting the axonal terminals of cholinergic afferents (Supplementary Fig. 5f). Optical stimulation was given through optical fibers implanted in mPFC to selectively activate halorhodopsin-expressing terminals and therefore inhibited the cholinergic inputs into mPFC. We found that the eNpHR3.0 expressing mice showed significantly impaired temporal order memory, whereas the mice with control virus remembered the serial presentation of two



objects (Fig. 5g, mCherry, 0.47 ± 0.23 ; eNpHR3.0, -0.0019 ± 0.09). These data together suggest that the SI/nBM-mPFC cholinergic circuit is required for temporal order recognition.

Moreover, we examined whether the MS-hippocampus (HP) cholinergic circuit is required for temporal order recognition memory. Using the same method described above, we bilaterally injected Cre-

dependent hm4D-mCherry AAV-Retro virus or the control virus into HP of ChAT-Cre mice, which would retrogradely transport to MS and inhibit the activity of MS cholinergic neurons (Fig. 5h and Supplementary Fig. 5g). In contrast to the SI/nBM-mPFC circuit, inhibition of MS-HP cholinergic projection did not change the discrimination ratio in the temporal order test (Fig. 5i, mCherry, 0.30 ± 0.07 ; hm4D,

Fig. 4 | Decreased ACh release in mPFC underlies defective temporal order recognition in *Ngfr*^{-/-} mice. **a** Schematic diagram depicting the measurement of relative ACh levels by a fluorescent ACh3.0 sensor. Fiber photometry was used for recording the fluorescence response of ACh sensor during sample 1, sample 2, and test phase in temporal order recognition test. **b** Fluorescence of AAV-ACh3.0 expressed in the mPFC. Scale bar, 1 mm. **c** Pseudocolored fluorescence responses of ACh3.0 in mPFC during object encounters (time 0) in each phase of the temporal order recognition test. Phasic ACh release was absent in *Ngfr*^{-/-} mice. Color scale indicates $\Delta F/F_0$. **d** Averaged ACh release upon object encounters (time 0). Thick lines indicate the averaged values between trials and the shaded areas represent SEM. **e** Group summary of peak ACh signals indicates no significant difference in

ACh release when the mice explored the two identical objects in sample phases. ACh signals were significantly higher when the mice explored the earlier object from sample phase 1 (green circle) than that when they explored the later object from sample phase 2 (purple square). Sample phase 1, $p = 0.54$; sample phase 2, $p = 0.97$; test phase, $p = 0.044$. *Ngfr*^{+/+}, $n = 3$; *Ngfr*^{-/-}, $n = 3$. **f** Group summary of peak ACh signals during object interaction indicate significantly reduced ACh release in each phase of the temporal order recognition in *Ngfr*^{-/-} mice. Sample phase 1, $p = 0.013$; sample phase 2, $p = 0.023$; test phase, $p = 0.0063$. *Ngfr*^{+/+}, $n = 3$; *Ngfr*^{-/-}, $n = 3$. Numerical data are means \pm SEM. Statistical analyses were performed by unpaired two-sided *t*-test in (e) and (f). * $p < 0.05$; ** $p < 0.01$; ns not significant. Source data are provided as a Source Data file.

0.34 ± 0.03). Taken together, only the specific cholinergic projection from SI/nBM to mPFC, but not MS to HP, plays a critical role in the temporal order memory.

A depolarizing shift of GABAergic inputs to mPFC in *Ngfr*^{-/-} mice

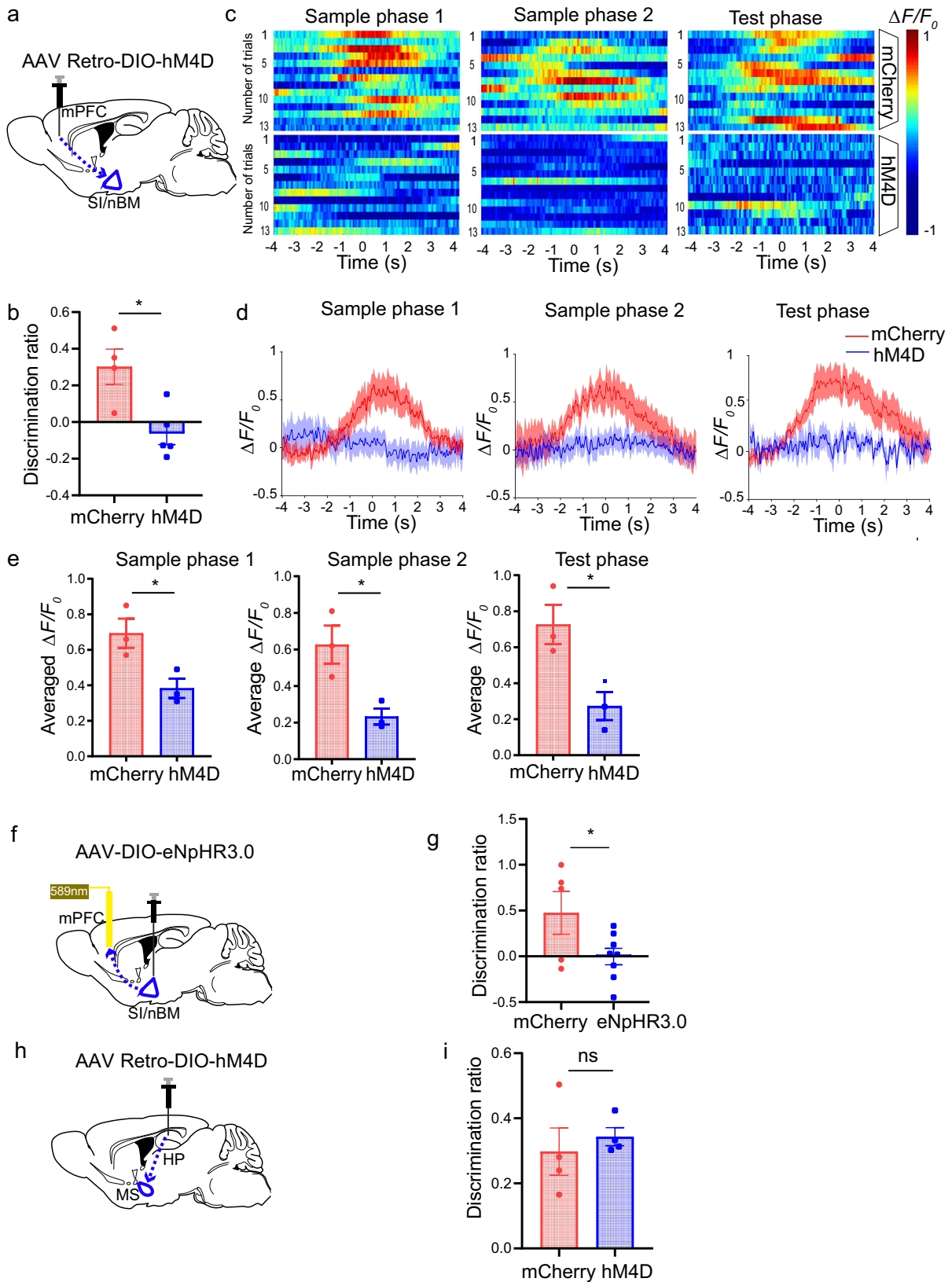
How does SI/nBM cholinergic projection regulate the activity of mPFC neurons? ACh is known to modulate synaptic activity and neuronal excitability^{13,41}. Thus, we measured both inhibitory and excitatory synaptic inputs onto mPFC layer V pyramidal neurons, which receive most of the ACh afferents from SI/nBM¹³. Whole-cell patch recorded miniature inhibitory postsynaptic currents (mIPSCs) in mPFC pyramidal neurons in the presence of the voltage-gated sodium channel blocker tetrodotoxin (TTX, 1.5 μ M), the NMDA receptor antagonist 2R-amino-5-phosphonovaleric acid (APV, 50 μ M) and the AMPA receptor antagonist 6-cyano-7-nitroquinoxaline-2,3-dione (CNQX, 50 μ M) at a holding potential of -70 mV (Supplementary Fig. 6a). Neither the amplitude nor the frequency (inter-event interval) of mIPSC was different between *Ngfr*^{+/+} and *Ngfr*^{-/-} mPFC (Supplementary Fig. 6b, c, amplitude, *Ngfr*^{+/+}, -45.4 ± 5.6 ; *Ngfr*^{-/-}, -37.1 ± 4.8 ; inter-event interval, *Ngfr*^{+/+}, 210.4 ± 14.6 ; *Ngfr*^{-/-}, 205.7 ± 10.9). Similarly, there was no difference in the amplitude or frequency of miniature excitatory postsynaptic currents (mEPSCs) measured in the presence of TTX (1.5 μ M) and the GABA receptor antagonist picrotoxin (80 μ M) (Supplementary Fig. 6d–f, amplitude, *Ngfr*^{+/+}, -12.4 ± 1.2 ; *Ngfr*^{-/-}, -12.7 ± 0.7 ; inter-event interval, *Ngfr*^{+/+}, 323.8 ± 27.8 ; *Ngfr*^{-/-}, 348.9 ± 23.4). Next, we measured synaptic strength by recording input/output curves of evoked synaptic responses. An extracellular stimulating electrode was placed at layer II/III and whole-cell recordings were made from mPFC layer V pyramidal neurons (holding potential, -70 mV). We observed no alteration in the amplitude of evoked IPSCs or that of evoked EPSCs between *Ngfr*^{+/+} and *Ngfr*^{-/-} mice, using a number of different stimulus intensities (Supplementary Fig. 6g, h). Finally, we measured the excitability of mPFC layer V pyramidal neurons in response to depolarizing current injection of increasing intensities. Pyramidal neurons from *Ngfr*^{+/+} and *Ngfr*^{-/-} mice exhibited similar firing frequencies over a wide range of depolarization steps (Supplementary Fig. 6i, j). Taken together, these results suggest deficiency in ACh release in mPFC as a consequence of NGFR disruption does not alter the number or strength of inhibitory or excitatory synapses, nor does it change the intrinsic excitability of pyramidal neurons in mPFC.

There is also evidence suggesting that cholinergic activity determines the excitatory or inhibitory state of GABAergic signaling⁴². We therefore examined whether the polarity of GABAergic inputs to mPFC pyramidal neurons was altered in *Ngfr*^{-/-} mice. Layer V pyramidal neurons of mPFC were patched at different holding potentials (V_{Hold}), in the presence of 50 μ M APV and 50 μ M CNQX, to determine at which V_{Hold} the GABAergic input switched from hyperpolarizing to depolarizing (Fig. 6a). To avoid perturbing the intracellular chloride gradient, recordings were made using the gramicidin perforated-patch configuration⁴³. In the voltage-clamp mode, we found a dramatic depolarizing-shifted reversal potential of GABA_A-mediated inhibitory postsynaptic currents (E_{IPSCs}) from -91.0 ± 2.1 mV in *Ngfr*^{+/+} slices to

-59.6 ± 3.8 mV in *Ngfr*^{-/-} slices (Fig. 6b), whereas no changes in RMP were observed under current-clamp recording configuration (Fig. 6c, *Ngfr*^{+/+}, -74.4 ± 0.64 ; *Ngfr*^{-/-}, -72.4 ± 0.97). The polarity of GABAergic driving force was determined by subtracting RMP from E_{IPSCs} . To this end, the GABAergic driving force was hyperpolarizing in the *Ngfr*^{+/+} mice, but became depolarizing-shifted in the *Ngfr*^{-/-} mPFC (Fig. 6d, *Ngfr*^{+/+}, -16.6 ± 2.2 ; *Ngfr*^{-/-}, 12.9 ± 3.6). These results suggest that loss of NGFR leads to a dramatic depolarizing shift of GABAergic polarity.

We next measured the impact of shift in GABAergic polarity on cortical network excitability. Cell-attached recordings were performed to record carbachol-induced firing (Fig. 6e, 10 μ M). We observed that carbachol-induced action potential frequency was much higher in *Ngfr*^{-/-} mice, as compared with that observed in *Ngfr*^{+/+} mice (Fig. 6f, *Ngfr*^{+/+}, 2.5 ± 0.2 Hz; *Ngfr*^{-/-}, 4.7 ± 0.5 Hz). Isoguvacine, a GABA agonist, effectively ceased cortical firing in *Ngfr*^{+/+} mice, with ceased firing periods as long as 35.7 ± 1.8 s. By contrast, isoguvacine only exerted a weak inhibition of cortical firing in *Ngfr*^{-/-} mice, with ceased firing period of 12.0 ± 2.3 s (Fig. 6g). In addition to carbachol, we used 12 μ M NMDA to induce mPFC pyramidal neuronal firing to examine whether NMDA-induced firing was inhibited by GABA agonist isoguvacine (Supplementary Fig. 7a). As shown in Supplementary Fig. 7b, in steady-state, NMDA-induced firing frequency in *Ngfr*^{-/-} mice was similar to that in *Ngfr*^{+/+} mice (*Ngfr*^{+/+}, 2.4 ± 0.5 Hz; *Ngfr*^{-/-}, 2.4 ± 0.3 Hz). After puffing isoguvacine, ceased firing period was significantly shorter in *Ngfr*^{-/-} mice than that in *Ngfr*^{+/+} mice (Supplementary Fig. 7c, *Ngfr*^{+/+}, 22.2 ± 3.5 s; *Ngfr*^{-/-}, 12.7 ± 1.9 s). The carbachol-induced firing frequency of layer V pyramidal cells was increased in *Ngfr*^{-/-} mice as compared to control mice, whereas NMDA-induced firing frequency was not affected in *Ngfr*^{-/-} mice. We argue that long-term downregulation of cholinergic activity in *Ngfr*^{-/-} mice may lead to some changes in the various cholinergic receptors in this region. This compensatory effect may lead to increased firing upon carbachol treatment in *Ngfr*^{-/-} mice. However, in either carbachol-induced or NMDA-induced firing system, NGFR deficiency resulted in consistent disinhibition to GABAergic agonist isoguvacine. Taken together, these data reveal prominent GABAergic disinhibition in the mPFC of *Ngfr*^{-/-} mice.

Previous studies have shown that a depolarizing shift of GABAergic signaling in the hippocampus significantly impaired object location recognition^{44,45}. Next, we determined whether a depolarizing shift of GABAergic driving force in the mPFC also contributes to temporal order recognition impairment in *Ngfr*^{-/-} mice. The GABAergic reversal potential of E_{IPSCs} is determined by the surface expression of KCC2 and NKCC1 chloride co-transporters, which mediates chloride efflux and influx, respectively. During postnatal development, E_{IPSCs} shifts from depolarizing to hyperpolarizing due to a concomitant downregulation of NKCC1 and upregulation of KCC2^{42,46,47}. To alter GABAergic driving force in the wild-type mice, we applied furosemide, an inhibitor that preferentially blocks KCC2 but also has effects on NKCC1⁴⁸. Specifically, we bilaterally injected 2 mM furosemide through cannula into mPFC of adult wild-type mice (3 months old), and performed three types of recognition memory tests. Remarkably, mPFC delivery of furosemide specifically attenuated temporal order



recognition (Supplementary Fig. 7d, test phase, saline, 0.32 ± 0.08 ; furosemide, -0.13 ± 0.20), but not novel object recognition (Supplementary Fig. 7e, test phase, saline, 0.48 ± 0.10 ; furosemide, 0.56 ± 0.27) or object location memory (Supplementary Fig. 7f, test phase, saline, 0.47 ± 0.06 ; furosemide, 0.46 ± 0.09). These data suggest that the polarity of GABAergic signaling in mPFC controls

recognition memory and strengthens the specific role of mPFC in the temporal order recognition, but not novel object and object location recognition.

In parallel, we determined whether the shift of E_{IPSCs} in *Ngfr*^{-/-} mice was attributable to changes in the expression of chloride co-transporters. Western blot revealed a significant reduction in KCC2

Fig. 5 | Inhibition of ACh release in the SI/nBM-mPFC circuit impairs temporal order recognition. **a** Schematic diagram illustrating chemogenetic inhibition of SI/nBM to mPFC cholinergic projection by injection of Cre-dependent hM4D-mCherry AAV-Retro or control virus in ChAT-Cre mice. **b** Discrimination ratio of temporal order recognition decreased in the hM4D group. $p = 0.012$. mCherry, $n = 4$; hM4D, $n = 5$. **c** Pseudocolored fluorescence responses of ACh3.0 in mPFC during object encounters (time 0) in each phase of the temporal order recognition test for the mCherry and hM4D group. **d** Reduction in averaged ACh release upon object encounters in hM4D group in each phase of the temporal order recognition test. Thick lines indicate the averaged values of trials and the shaded areas represent SEM. **e** Group summary of peak ACh signals indicates reduced ACh release in hM4D group during object encounters. Sample phase 1, $p = 0.035$; sample phase 2, $p = 0.025$; test phase, $p = 0.028$. mCherry, $n = 3$; hM4D, $n = 3$. **f** Diagram of

optogenetic inhibition of cholinergic projection from SI/nBM to mPFC. AAV9-DIO-eNpHR3.0, or control virus were injected into SI/nBM of ChAT-Cre mice. After 4 weeks, 589 nm light was applied through an optical fiber planted in mPFC to inhibit cholinergic terminals. **g** Decreased discrimination ratio in temporal order recognition by optogenetic inhibition of SI/nBM to mPFC cholinergic innervation. $p = 0.047$. mCherry, $n = 5$; eNpHR3.0, $n = 8$. **h** Schematic diagram depicting specific inhibition of MS to HP cholinergic projection by injection of Cre-dependent hM4D-mCherry AAV-Retro or control virus in ChAT-Cre mice. **i** Intact discrimination ratio in temporal order recognition after chemogenetic inhibition of MS to HP cholinergic projection. $p = 0.58$. mCherry, $n = 4$; hM4D, $n = 4$. Numerical data are means \pm SEM. Statistical analyses were performed by unpaired two-sided t -test in **(b)**, **(e)**, **(g)**, and **(i)**. $*p < 0.05$; ns not significant. Source data are provided as a Source Data file.

levels in the mPFC of *Ngfr*^{-/-} mice as compared to *Ngfr*^{+/+} mice (Fig. 6h, *Ngfr*^{+/+}, 1.0 ± 0.09 ; *Ngfr*^{-/-}, 0.53 ± 0.09). By contrast, NKCC1 expression in the mPFC of *Ngfr*^{-/-} mice was not altered (Fig. 6i, *Ngfr*^{+/+}, 1.0 ± 0.08 ; *Ngfr*^{-/-}, 0.99 ± 0.02). Thus, the reduced KCC2 levels may be responsible for the observed changes in GABAergic reversal potential in the mPFC of *Ngfr*^{-/-} mice.

Comparatively, we examined the E_{IPSCs} in the CA1 pyramidal neuron from *Ngfr*^{-/-} hippocampus. Consistent with the intact MS-HP cholinergic activity in the *Ngfr*^{-/-} mice, there was no difference in the E_{IPSCs} nor the GABAergic driving force between genotypes (Fig. 6j-l, RMP, *Ngfr*^{+/+}, -70.8 ± 0.78 mV; *Ngfr*^{-/-}, -70.4 ± 0.67 mV). Thus, GABAergic inputs onto the hippocampal pyramidal neurons were normal in the *Ngfr*^{-/-} mice.

ACh receptor agonist nicotine rescues defected temporal order recognition in *Ngfr*^{-/-} mice

If reduced ACh release from the SI/nBM-mPFC circuit led to reduced KCC2 expression, depolarizing shift of GABAergic driving force and impaired temporal order recognition in *Ngfr*^{-/-} mice, restoration of cholinergic activity should be able to rescue these phenotypes. ACh signaling is activated through muscarine or nicotine ACh receptors^{49,50}. We examined the effect of in vivo administration of nicotine in *Ngfr*^{-/-} mice, which could effectively permeate the blood-brain barrier^{51,52}. By subcutaneous injection of nicotine (2.5 mg/kg, s.c., 4 injections during the 12-h light cycle) over 14 consecutive days³³, we observed that KCC2 expression was significantly increased in the mPFC of *Ngfr*^{-/-} mice (Fig. 7a, Control, 0.77 ± 0.05 ; Nicotine, 1.09 ± 0.08). Furthermore, we investigated whether nicotine treatment would restore the depolarizing shift of the reversal potential of E_{IPSCs} and rescue the impairment in temporal order memory in *Ngfr*^{-/-} mice. To reduce the potential stress effect of daily subcutaneous injection on animal behaviors, nicotine was given in the drinking water at the dose of 650 μ g/ml over 4-week period. Perforated-patch recordings of mPFC layer V pyramidal neurons revealed a dramatic reversal of the depolarizing-shifted E_{IPSCs} , from -79.23 ± 3.79 mV to -109.5 ± 6.41 mV in the *Ngfr*^{-/-} mPFC, closer to that from wild-type mPFC (Fig. 7b-e, RMP, Control, -67.58 ± 3.55 ; Nicotine, -72.77 ± 2.57). Remarkably, the discrimination ratio was 0.008 ± 0.05 for *Ngfr*^{-/-} mice treated with vehicle, but 0.31 ± 0.11 for those treated with nicotine, indicating a significant improvement of temporal order recognition (Fig. 7f, g). No significant difference in temporal order recognition for nicotine-treated wild-type mice corroborates the notion that specific cholinergic deficiency underlies impaired recency judgment in *Ngfr*^{-/-} mice (Supplementary Fig. 7g, Test phase, Control, 0.21 ± 0.07 ; Nicotine, 0.08 ± 0.06). Taken together, these results suggest that activation of cholinergic pathway restores GABAergic driving force and temporal order recognition deficits in *Ngfr*^{-/-} mice.

Discussion

The goal of the present study is to investigate the functional specificity of BF cholinergic subpopulations and determine the circuitry and

molecular mechanisms underlying the cholinergic control of recognition memory. We have taken advantage of single-cell RNA sequencing data with systematic survey of cell types in the mouse nervous system and identified the molecular markers for cholinergic neurons from different anatomic boundaries. Interestingly, NGFR specifically defines BF cholinergic projection neurons, which broadly innervate cortical and subcortical regions and modulate a plethora of cognitive function. We thus employed the *Ngfr* knockout mouse model and investigate its regulatory role in cholinergic circuits. A number of interesting discoveries were made in this study. First, we showed that NGFR specifically regulated the excitability of cholinergic neuron in the SI/nBM-mPFC circuit, but not MS-HP pathway. Second, *Ngfr*^{-/-} mice exhibited prominent impairment in temporal order recognition memory, whereas the other forms of recognition memory were intact. Expression of *Ngfr* in the *Ngfr*^{-/-} SI/nBM rescued impaired temporal order memory. Third, using a genetic sensor ACh3.0 with millisecond temporal resolution, we demonstrated that ACh release in mPFC not only predicted object encounters but also mediated recency judgments of objects during temporal order recognition, whereas diminished ACh release was seen in *Ngfr*^{-/-} mice. Fourth, by using chemogenetic and optogenetic tools, we demonstrated that SI/nBM-mPFC circuit was essential for temporal order recognition memory. Finally, electrophysiology recording revealed a depolarizing shift of GABAergic inputs to *Ngfr*^{-/-} mPFC pyramidal neurons, which was in parallel with downregulated KCC2 levels. Conversely, potentiation of ACh signaling increased KCC2 levels, restored GABAergic driving force and rescued temporal order recognition memory deficits in *Ngfr*^{-/-} mice. Taken together, these results highlight the critical role of NGFR in regulating the SI/nBM-mPFC cholinergic circuit, which is fundamental to temporal order recognition memory.

The function of NGFR has been well studied in the peripheral nervous system⁵⁴⁻⁵⁶, as well as during early brain development^{17-20,57}. The “Yin and Yang” theory of neurotrophins denotes that NGFR acts as a negative regulator for neuronal survival and synaptic competition⁵⁸. Interestingly, we found that *Ngfr* is specifically enriched in the BF cholinergic projection neuron in the adult nervous system, but not in the cholinergic neuron residing in the striatum, thalamus, and cortex. Moreover, previous studies reported impaired cognitive function in the BF cholinergic neuron-specific *Ngfr* knockout mice³¹. To resolve the seemingly contradiction arising from the apparent high expression of *Ngfr* in certain cholinergic subpopulation versus its putative effect on cell death, we stratified the cholinergic neurons into *Ngfr*⁺ and *Ngfr*⁻ subpopulations and compared the DEGs. Biological process analysis of DEGs between these two subpopulations indicated that *Ngfr* is prominently involved in the regulation of neurotransmitter and synaptic signaling, rather than cell death. Indeed, electrophysiological recording revealed that loss of NGFR leads to reduced excitability of SI/nBM cholinergic subpopulation. Consistently, fiber photometry recordings revealed diminished ACh release in the *Ngfr*^{-/-} mPFC, a major target of SI/nBM projection, during object encounters and discrimination of objects in temporal order. By contrast, we found no significant

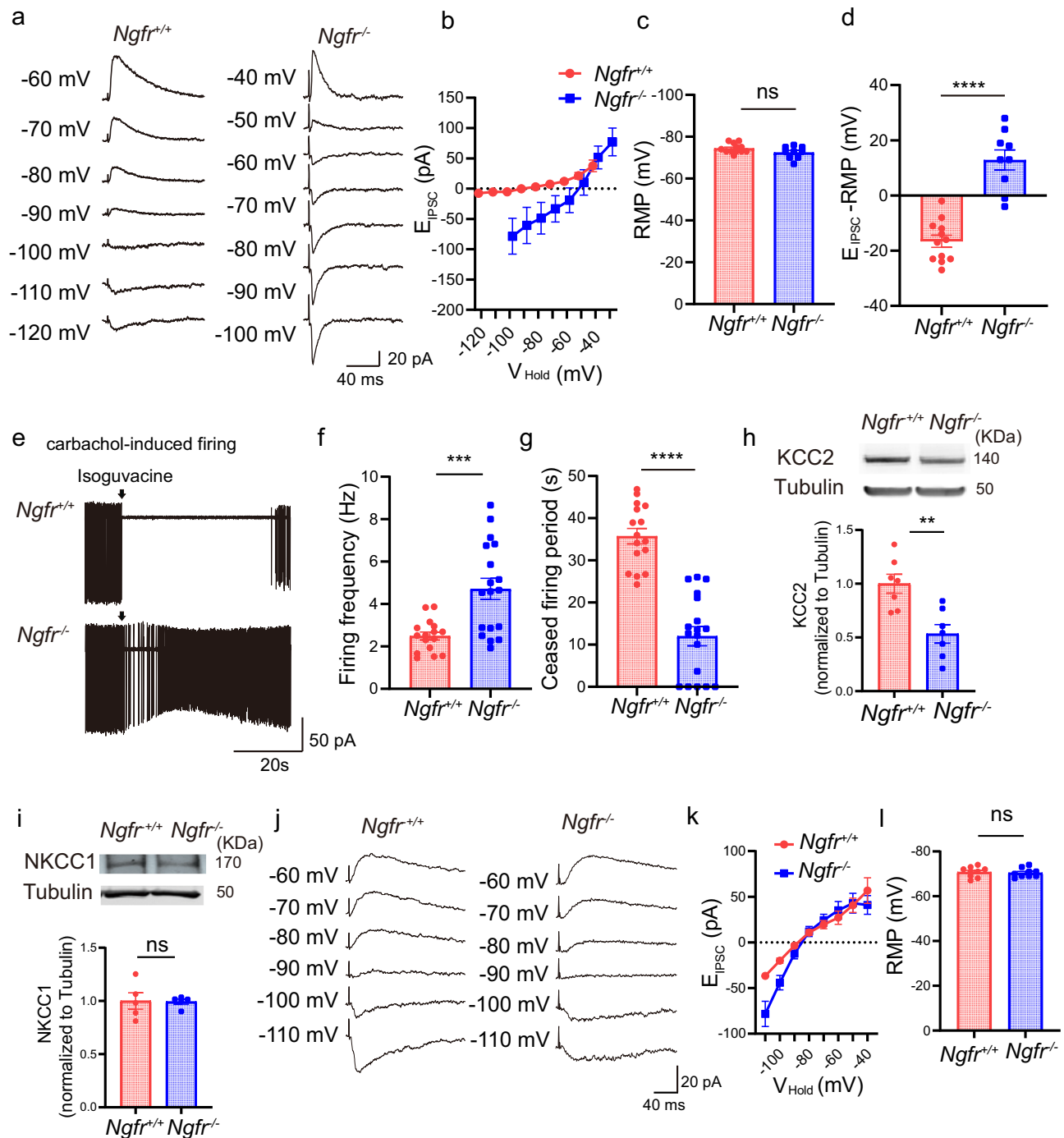
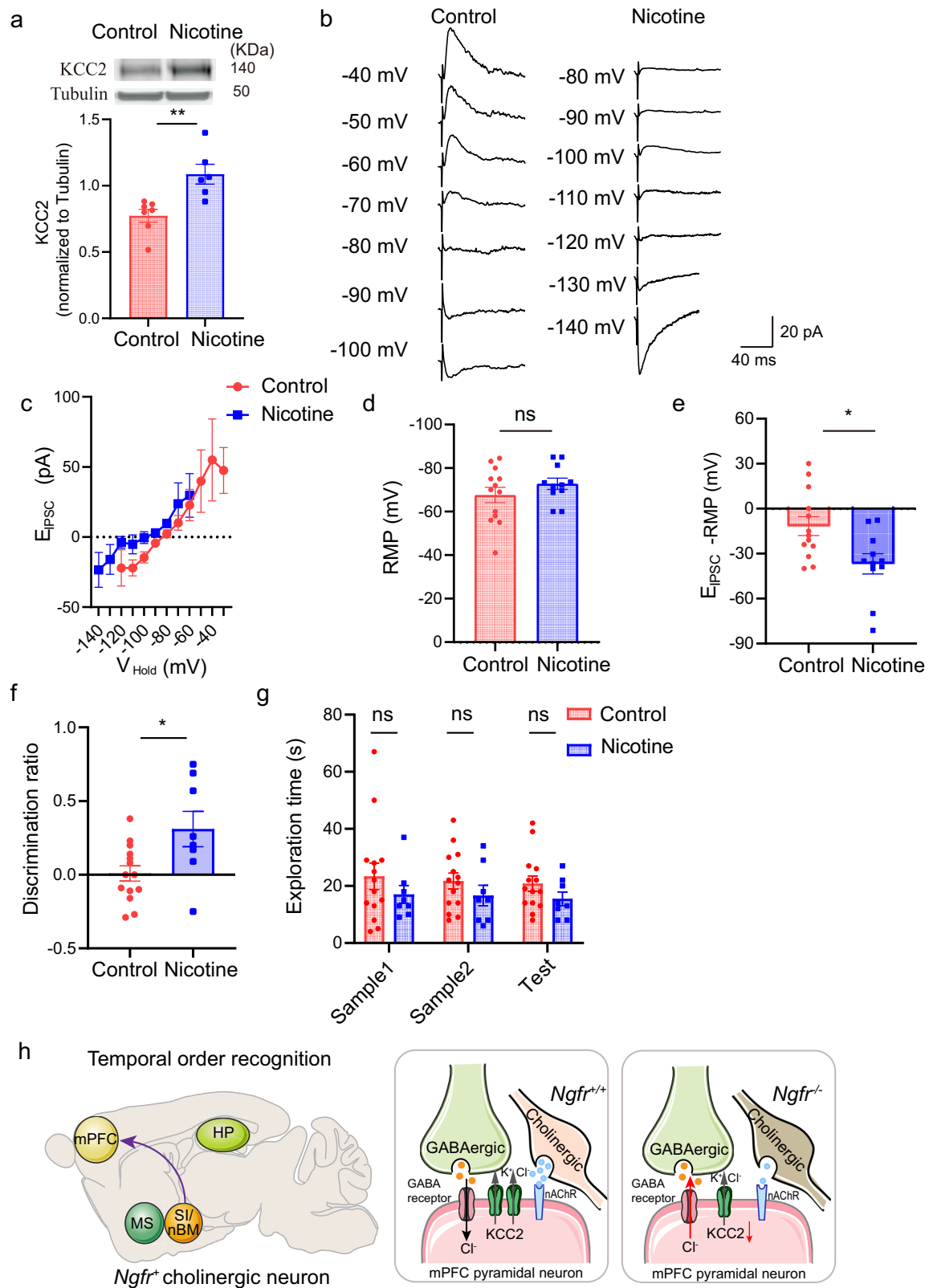


Fig. 6 | Depolarizing-shifted reversal potential of GABA_A-mediated E_{IPSCs} and reduced GABAergic inhibition in $Ngfr^{-/-}$ mPFC. **a Perforated patch recorded the reversal potential of E_{IPSCs} and resting membrane potential (RMP) in the layer V pyramidal neurons, in the presence of 50 μ M APV and 50 μ M CNQX. Representative traces indicate a depolarizing shift of E_{IPSCs} in $Ngfr^{-/-}$ mPFC. **b** Group summary suggests depolarizing shift of reversal potential of E_{IPSCs} in $Ngfr^{-/-}$ mice. $Ngfr^{+/+}$, $n = 12$ cells from 5 mice; $Ngfr^{-/-}$, $n = 9$ cells from 5 mice. **c** No differences of RMP in current-clamp mode between genotypes. $p = 0.095$. $Ngfr^{+/+}$, $n = 12$ cells from 5 mice; $Ngfr^{-/-}$, $n = 9$ cells from 5 mice. **d** Hyperpolarizing GABAergic driving force in $Ngfr^{+/+}$ mice, versus depolarizing-shifted GABAergic strength in $Ngfr^{-/-}$ mice. $p < 0.0001$. $Ngfr^{+/+}$, $n = 12$ cells from 5 mice; $Ngfr^{-/-}$, $n = 9$ cells from 5 mice. **e** Reduced GABAergic inhibition of layer V pyramidal neurons in $Ngfr^{-/-}$ mPFC. Cell-attached recordings of carchamol-induced firing. Representative traces of basal spike frequency and effects of puffing GABA agonist isoguvacine (100 μ M). **f** In steady-state, carchamol-induced firing frequency was significantly higher in $Ngfr^{-/-}$ mice. $p = 0.0004$. $Ngfr^{+/+}$, $n = 16$**

cells from 4 mice; $Ngfr^{-/-}$, $n = 18$ cells from 4 mice. **g** After puffing isoguvacine, ceased firing period was significantly shorter in $Ngfr^{-/-}$ mice. $p < 0.0001$. $Ngfr^{+/+}$, $n = 16$ cells from 4 mice; $Ngfr^{-/-}$, $n = 18$ cells from 4 mice. **h** Representative blots and quantification of KCC2 levels in mPFC. Significantly reduced KCC2 expression in $Ngfr^{-/-}$ mice. $p = 0.0026$. $Ngfr^{+/+}$, $n = 7$; $Ngfr^{-/-}$, $n = 7$. **i** Representative blots and quantification indicate intact NKCC1 expression in $Ngfr^{-/-}$ mPFC. $p = 0.93$. $Ngfr^{+/+}$, $n = 5$; $Ngfr^{-/-}$, $n = 5$. **j** Perforated patch recorded the reversal potential of E_{IPSCs} and RMP of hippocampal CA1 pyramidal neurons. **k** Intact reversal potential of E_{IPSCs} in CA1 pyramidal neurons of $Ngfr^{-/-}$ mice. $Ngfr^{+/+}$, $n = 9$ cells from 3 mice; $Ngfr^{-/-}$, $n = 9$ cells from 3 mice. **l** No difference of RMP between genotypes. $p = 0.75$. $Ngfr^{+/+}$, $n = 9$ cells from 3 mice; $Ngfr^{-/-}$, $n = 9$ cells from 3 mice. Numerical data are means \pm SEM. Statistical analyses were performed by unpaired two-sided t -test in (c), (d), (f–i), and (l). *** $p < 0.001$; **** $p < 0.0001$; ns not significant. Source data are provided as a Source Data file.



difference in the cell number of cholinergic neurons in SI/nBM between the adult *Ngfr*^{+/+} and *Ngfr*^{-/-} mice at the age we used for our experiments (3–7 months). It should be noted that previous studies reported either increased or decreased cell number of cholinergic neurons in the *Ngfr*^{-/-} MS/vDB^{28–30,39}. Whether loss of NGFR affects SI/nBM was not fully studied. We now show that SI/nBM exhibited similar number of ChAT⁺ cells in *Ngfr*^{+/+} and *Ngfr*^{-/-} mice. Thus, *Ngfr* may exert

differential effects on various cholinergic subpopulations, and in SI/nBM the primary function of NGFR is to regulate cholinergic excitability and ACh release, rather than controlling cell survival. Taken together, we have characterized a role of NGFR in the regulation of SI/nBM cholinergic neuron activity and ACh release.

Exactly how NGFR regulates the excitability of cholinergic neurons in SI/nBM and ACh release in mPFC remains elusive. It has been

Fig. 7 | ACh receptor agonist nicotine rescues defected temporal order recognition in *Ngfr*^{-/-} mice. **a** Subcutaneous injection of nicotine (2.5 mg/kg, s.c., 4 injections during the 12-h light cycle) over 14 consecutive days increased KCC2 expression in *Ngfr*^{-/-} mice. $p = 0.0041$. Control, $n = 7$; Nicotine, $n = 6$. **b** The reversal potential of E_{IPSCs} and resting membrane potential (RMP) was recorded in the mPFC layer V pyramidal neurons, in the presence of 50 μ M APV and 50 μ M CNQX. Representative traces indicate a hyperpolarizing shift of E_{IPSCs} in *Ngfr*^{-/-} mPFC after chronic treatment of nicotine over 4-week period. **c** Group summary of E_{IPSCs} suggest hyperpolarizing shift of reversal potential of E_{IPSCs} in *Ngfr*^{-/-} mice treated with nicotine. Control, $n = 13$ cells from 4 mice; Nicotine, $n = 10$ cells from 3 mice. **d** No difference of RMP in current-clamp mode between control and nicotine group. $p = 0.26$. Control, $n = 13$ cells from 4 mice; Nicotine, $n = 11$ cells from 3 mice. **e** Hyperpolarizing shift of GABAergic driving force after chronic nicotine treatment. $p = 0.013$. Control, $n = 13$ cells from 4 mice; Nicotine, $n = 11$ cells from 3 mice. **f, g** Chronic treatment of *Ngfr*^{-/-} mice with nicotine over 4-week period significantly

improved temporal order recognition, as indicated by the discrimination ratio, $p = 0.014$ (**f**). No difference in the exploration time of objects between treatments (**g**). Control, $n = 14$; Nicotine, $n = 8$. **h** Working model. *Ngfr*^{-/-} cholinergic projection from SI/nBM to mPFC selectively regulates temporal order recognition memory. Specifically, NGFR determines the intrinsic excitability of SI/nBM cholinergic projection neurons and tunes ACh release at cholinergic terminals in mPFC during object encounters and recency judgments. Impaired ACh release in *Ngfr*^{-/-} mPFC is associated with reduced KCC2 expression, GABAergic disinhibition, and deficits in recency judgment. This panel was partly generated using Servier Medical Art, provided by Servier, licensed under a Creative Commons Attribution 4.0 unported license. Numerical data are means \pm SEM. Statistical analyses were performed by unpaired two-sided *t*-test in (**a**), (**d–f**), and two-way ANOVA with Bonferroni's multiple comparisons in (**g**). * $p < 0.05$; ** $p < 0.01$; ns not significant. Source data are provided as a Source Data file.

reported that NGFR regulates the firing properties of sympathetic neurons through voltage-gated currents including the sodium current, the M-type, delayed rectifier, and calcium-dependent potassium currents⁶⁰. Moreover, neurotrophins including BDNF and NGF activate NGFR and increase the excitability of rat sensory neurons by enhancing TTX-resistant sodium current and suppressing a delayed rectifier-like potassium current⁶¹. We thus speculate that NGFR may control the excitability of BF cholinergic neuron by regulating the expression or the activity of ion channels, which warrants future studies.

Another important finding of this study is that the SI/nBM-mPFC innervation plays a critical role in temporal order recognition memory. Previous studies have suggested that BF cholinergic neuron exerts broad control over cortical regions and regulates physiological processes including attention, learning, and memory^{62–65}. Deficits in cholinergic inputs lead to neurodegenerative diseases, mood disorder, and chronic pain^{66,67}. A whole-brain atlas for the cholinergic system has also been mapped⁶⁸. However, the specific cholinergic circuit that mediates different types of recognition memory and the critical molecule that determines the cholinergic activity remain elusive. Previously, a major obstacle in the study of cholinergic circuits and activities lies in the lack of ACh sensors with high spatiotemporal resolution. Because of this technical limitation, the release of ACh was thought to be “slow” and “tonic”⁶⁹. Choline oxidase-coated microelectrodes have been used to detect the concentration of choline, the decomposition product of ACh^{70–72}. However, this method was limited by low sensitivity and potential disturbance of endogenous ACh homeostasis. To monitor the ACh kinetics in the mPFC during the recognition memory task, we have applied an optimized ACh sensor 3.0 for real-time tracing of the cholinergic activity in vivo⁴⁰.

A number of interesting findings were made using the ACh sensor. First, we found that ACh release in the mPFC was tightly associated with object encounters, the first step in the object recognition process. Intriguingly, the ACh signals in mPFC rose a few seconds before the interaction with objects, and declined rapidly when the mice withdrew from exploring the objects. These results imply that the phasic ACh release in mPFC is required for the recognition of objects and the rise of ACh signals predicts the time for response. Second, we have quantitatively compared the strength of ACh release when the mice explore the earlier object versus the later object. The ACh signals in the sample phase 1 and 2, in which the mice explored two identical objects, were equal. Remarkably, during the test phase, there was a lot more ACh release when the animals explored the earlier object than that of the later object. These data suggest that ACh signal not only predicts object encounter, but also directly determines recency judgments of objects. Third, in contrast to temporal order recognition, ACh signals in the mPFC during novel object recognition and object location were detected only in the sample phase but not in the test phase. These data suggest that ACh signals in mPFC are not involved in the memory retrieval of novel object and object location recognition. Fourth,

although *Ngfr*^{-/-} mice exhibited reduced ACh signals in the sample phase of novel object and object location recognition, the behavioral outcomes of these two types of recognition remained intact. We speculate that defected ACh release in mPFC during the encoding stage of recognition may not be sufficient to interrupt discrimination of object familiarity or spatial recognition. Indeed, lesions in the mPFC per se do not affect novel object and object location recognition². Measurement of ACh release in other brain regions, such as perirhinal cortex or hippocampus, during novel object and object location recognition, warrants future studies. Taken together, our findings highlight the pivotal role of *Ngfr*-dependent ACh release in the mPFC in temporal order recognition memory, but not in novel object or object location recognition.

Human imaging studies^{73–75} and nonhuman primate lesion studies^{76,77} demonstrate mPFC as a critical brain region for recognition memory. The lesion studies in rats further reveal a key role of mPFC in temporal order memory task^{3,38}. The selective ablation studies also suggest that the perirhinal cortex, the hippocampus and the mPFC must work together to ensure proper temporal order memory^{3,4,78}. In this study, we have delineated the SI/nBM-mPFC cholinergic circuit in the regulation of temporal order recognition memory, and illustrated the functional significance of NGFR in this specific circuit. In terms of the correlation between *NGFR* and neurological diseases, genome-wide association analysis revealed *NGFR* SNP rs2072446 is associated with AD risk⁷⁹. Moreover, *NGFR* SNP rs11466125, rs2072446, and rs11466162 are indicative of the risk of schizophrenia^{80,81}. We thus define a specific NGFR-dependent SI/nBM-mPFC cholinergic circuit in the regulation of a specific type of recognition memory and suggest its implication in neurological and psychiatric diseases.

In addition to the observation that NGFR is critical for the cholinergic activity in the SI/nBM-mPFC innervation, we suggest the functional significance of reduced ACh release on cortical synaptic plasticity. Remarkably, we found that it is the transmembrane chloride gradients-mediated GABAergic driving force, but not the inhibitory synaptic inputs impinging on pyramidal neurons in the mPFC, that is affected by the disrupted *Ngfr*^{-/-} cholinergic innervation. It has been well established that the efficacy of GABAergic inhibition is not only mediated by GABA receptors, but also determined by the transmembrane chloride gradient. The dynamics of electrochemical gradient of chloride are regulated by the chloride transporters NKCC1 and KCC2, which function as the neuronal importer and exporter of chloride, respectively⁸². During the developing process of interneuron migration into the cortical layers, the low expression of KCC2 and high expression of NKCC1 elicits membrane depolarization and calcium influx upon GABA exposure^{83,84}. Then, the functional switches of GABA occur after the first postnatal week in the rodent cortex, due to the physiological upregulation of KCC2 and downregulation of NKCC1 expression by nicotinic cholinergic activity⁴². Remarkably, either mutations in the regulatory domain of *KCC2* or reduced expression of

KCC2 is identified in autism, schizophrenia, tuberous sclerosis complex, focal cortical dysplasia, epilepsy, and Rett syndrome^{82,85–87}. As the convergent mechanism of these neurological disorders, reduced KCC2 expression results in excessive intraneuronal chloride levels and excitation/inhibition imbalance in neural circuits. In our study, a series of experiments demonstrated a depolarizing shift of GABAergic reversal potential, and impaired GABAergic inhibition on cortical firing in parallel with reduced KCC2 expression in *Ngfr*^{-/-} mice. Further, we determined that changes in the polarity of GABAergic signaling in the *Ngfr*^{-/-} mPFC contribute to the impairment in temporal order recognition. We used furosemide, an inhibitor that preferentially blocks KCC2 but also has effects on NKCC1, to alter the GABAergic driving force in the wild-type mPFC. We found that delivery of furosemide to the mPFC of adult wild-type mice specifically attenuated temporal order recognition, but not novel object recognition or object location recognition, an effect similar to that seen in *Ngfr*^{-/-} mice with reduced KCC2 expression in mPFC. These inextricably linked molecular and cellular events underlie the mechanism of temporal order recognition memory deficits in *Ngfr*^{-/-} mice. Moreover, we provide evidence that potentiation of ACh signaling upregulates KCC2 levels, restores GABAergic driving force, and rescues temporal order recognition memory deficits. Therefore, we delineate a molecular pathway underlying the cholinergic regulation of GABAergic polarity and temporal order recognition.

The differential effects of NGFR on ACh release by SI/nBM and MS cholinergic neurons deserve further investigations. Although these two BF subpopulations all express NGFR, they show comprehensive difference in nature. First, SI/nBM cholinergic neuron is early-born in the embryonic day, whereas the MS subcluster is late-born. The differentiation and migration of these two subpopulations are under the control of distinct group of transcriptional factors⁸⁸. Second, SI/nBM subpopulation is caudally located and primarily projects to the cortical regions, whereas the MS neuron is rostrally located and mainly projects to the hippocampus⁸⁹. Third, distinct cholinergic outputs of these two subpopulations lead to difference in the retrograde signals and target-specific cues, such as growth factors (NGF, BDNF, CNTF, NT3) and morphogens (SHH, RA, FGF8, BMP9)¹¹, which in turn affect cholinergic differentiation⁹⁰. Thus, in terms of nature and nurture, the SI/nBM and MS cholinergic neurons show broad heterogeneity. Moreover, it has been reported that BF cholinergic neurons show distinct patterns of firing modes, synchronization and behavioral correlates^{15,91,92}. It thus complicates the regulatory role of NGFR on the excitability of these two distinct subtypes of cholinergic neurons. In addition to the diverse effects of NGFR's regulation on cholinergic soma, differential effects of NGFR on cholinergic axons either innervating to the cortex or the hippocampus have also been reported³⁰. Thus, further studies that reveal differences in gene expression patterns of the SI/nBM and MS subpopulations may provide insights to the intricate effect of NGFR regulation.

In conclusion, we identify that NGFR-dependent SI/nBM-mPFC cholinergic circuit regulates temporal order recognition memory, and illustrate the mechanism that ACh signaling determines the polarity of GABAergic transmission. These results may provide insights into the functional specificity of the cholinergic subpopulation.

Methods

Mice models

Ngfr knockout mice⁹³ from Jackson Laboratories (stock number: 002213) were backcrossed into C57BL/6 genetic background over 15 generations. Adult *Ngfr* knockout (*Ngfr*^{-/-}) and wild-type (*Ngfr*^{+/+}) males were littermates derived from a heterozygous (*Ngfr*^{+/-}) mating strategy. To conduct electrophysiology study of cholinergic neurons, *Ngfr* mice in C57BL/6 were crossed with ChAT-EGFP mice⁹⁴ in Swiss-Webster (kindly provided by Dr. Hermes Yeh) for more than five generations. To perform behavioral studies, mice backcrossed to C57BL/6 background

for over five generations were used. Animals were group housed (2–4 animals/cage) in a climate-controlled animal facility (22 ± 2 °C), maintained on a 12-h light/dark cycle. All procedures were approved by the Animal Care and Use Committees of Tsinghua University. The behavioral and electrophysiological experiments were performed in male mice, owing to cyclic hormone effects of female mice. The molecular biology and photometry experiments were performed in both male and female mice.

Locomotor activity, novel object, object location, and temporal order recognition tests

The behavior tests for rat recognition memory have been previously described³ and we used the same procedure in our mice. Experiments were conducted in male mice, at the ages of 3–7 months old, during the light phase. On testing days, mice were habituated in a room adjacent to the testing room for 1 h prior to testing. On day 1, mice were habituated to the experimental apparatus consisting of a Plexiglas Digiscan automated open field (Accuscan; 42 × 42 × 30 cm) under red-light illumination (7 ± 2 lux). The mice were allowed to freely explore the open field for 1 h and the total distance traveled, in 5-min time intervals, was recorded. The next day, mice were examined in the temporal order recognition test in the same apparatus. The temporal order recognition test measures the mouse's ability to differentiate between two familiar objects presented at different intervals. The test was run in three 5-min sessions. For all three sessions, mice were placed in the same apparatus from the locomotor activity test the day before. There was 1 h time period between the first (Sample 1) and second session (Sample 2), and a 3-h time period between the second and third (Test) sessions. For the first session, mice were placed in the apparatus with two identical objects and allowed to explore. During the second session, mice were presented with a different set of identical objects. During the third session, mice were placed with duplicates of each object from the previous two sessions. If temporal order memory is intact, mice will spend more time exploring the object from sample phase 1 compared with the object from sample phase 2. The animal performance in temporal order recognition memory was assessed by discrimination ratio. The discrimination ratio was calculated as the difference in time spent by each animal exploring the object from sample phase 1 compared with the object from sample phase 2 divided by the total time spent exploring both objects during the test period. The objects consisted of two rectangular boxes (3 × 3 × 6 cm), or two laboratory flasks (4 × 6 cm), each either black or white. The objects were placed in two corners of the open field apparatus, 8 cm from the side walls. The positions of the objects in the test and the objects used in the different phases were counterbalanced between the genotypes. Each session was video recorded using a Sony Handycam with the experimenter absent from the room during the test. Time spent exploring each object was subsequently scored from the videotapes with EthoVision XT 16 (Noldus). Exploration time was recorded as the number of seconds when each mouse was facing the object with its nose within 2 cm of the object. Mice with total exploration time <3 s were excluded from further analyses.

For the object location recognition, mice were placed into the open field for a 10-min period where they were allowed to explore two identical copies of an object. One hour later, mice were returned to the arena for the 5-min test phase and allowed to explore one copy of the object in the same location as that in the sample phase and one copy of the object in a novel location.

For the novel object recognition, mice were placed into the arena for a 10-min period where they were allowed to explore two identical copies of an object. One hour later, mice were placed back into the open field for 5 min, with a copy of the object encountered previously and a copy of a novel object. The novel object differed from the familiar object in both color and shape.

Experiments and data analyses were conducted by experimenters who were blinded to the genotype and experimental groups.

Single-cell RNA sequencing analysis

Single-cell RNA sequencing data were downloaded from the DropViz³⁴ and the Mousebrain datasets³⁵, respectively. Cell clusters annotated with the expression of *Chat* were extracted. For the DropViz dataset, the clusters of GP_1-1, GP_1-2, TH_1-1, PC_4-8, FC_1-5, and STR_12-1 were used. For the Mousebrain dataset, the clusters of TECHO for striatum, DECHO1 for BF, DECHO2 for thalamus, and TEINH4 for cortex were used. The isolated cell cluster from the cortex with no expression of *Chat* was excluded. Low quality cells have been filtered in the original datasets. In each dataset, read matrix from different clusters were re-clustered with the Seurat package (v4.3.0.1)⁹⁵. PCA analysis was carried out and the top 20 principal components were used. Cell clusters were identified with the function of FindClusters by setting the resolution threshold as 1.0. The brain regions for cells (BF, striatum, thalamus, cortex) were noted from the original datasets.

The differential expression analysis of single-cell RNA sequencing data was done by Seurat using the function of FindAllMarkers (Wilcoxon rank-sum test, *p* value adjusted by FDR). Genes with adjusted *p* value <0.05 were taken as DEGs. The UMAPs and DEGs heatmap were drawn using the plot functions of Seurat. GSEA analysis was done by clusterProfiler (v4.7.1.2) using the Gene Ontology database⁹⁶.

Preparation and maintenance of brain slices

Ngfr^{+/+} and *Ngfr*^{-/-} mice at the ages of postnatal weeks of 7–10 were used in this study. The mice were sacrificed with a guillotine after being administered with isoflurane. The brains were quickly removed, and 300 μ m-thick coronal slices containing mPFC or BF were cut on a Compressome (VF-200, Presinary, Greenville, NC). The slices were cut in oxygenated ice-cold Na⁺-free sucrose solution containing 2.5 mM KCl, 1.25 mM NaH₂PO₄, 26 mM NaHCO₃, 0.5 mM CaCl₂, 4.0 mM MgCl₂, 10 mM glucose, and 250 mM sucrose. The slices were initially incubated at 34 °C in ACSF containing 125 mM NaCl, 2.5 mM KCl, 1.25 mM NaH₂PO₄, 2 mM CaCl₂, 1 mM MgCl₂, 26 mM NaHCO₃, and 10 mM glucose, bubbled with carbogen gas (95% O₂–5% CO₂, pH 7.4), and then kept at room temperature. Slices were allowed to recover for at least 60 min before experiments were started.

Electrophysiological recordings

After recovery, the mPFC or the BF slices were transferred into a recording chamber at -32–34 °C. For the current clamp, the recording pipettes were filled with intracellular solution containing (in mM) 130 K-gluconate, 1 MgCl₂, 5 EGTA, 5 MgATP, 10 HEPES and 0.4 Na₂GTP (pH 7.2 with KOH). The resistances of patch pipettes were 3–6 M Ω . The mEPSCs were recorded with a holding potential at -70 mV in the presence of 80 μ M picrotoxin and 1.5 μ M TTX to block GABA_A receptor currents and voltage-gated sodium currents, respectively. To record mIPSCs, Cs⁺-based intracellular solution (140 mM CsCl₂, 2 mM MgCl₂, 2 mM Na₂-ATP, 0.5 mM Na₂GTP, 5 mM Na₂-phosphocreatine, 1 mM EGTA, 10 mM HEPES, and 5 mM QX-314, pH 7.25 with CsOH) was used. The mIPSCs were recorded at -70 mV in the presence of 50 μ M CNQX, 50 μ M APV, and 1.5 μ M TTX. The access resistance was monitored during recordings, and the data were excluded from analysis if the series resistance changed more than 20% from control levels.

Perforated-patch recordings were made from identified pyramidal neuron at layer V of mPFC and the extracellular stimulating electrodes were placed at mPFC layer II/III. Recording electrodes (4–5 M Ω) contained 80–100 μ g/ml gramicidin in a solution comprised of the following (in mM): 140 KCl, 1 MgCl₂, 4 MgATP, 0.5 EDTA, 10 HEPES, pH 7.2. The electrode tip was front-filled with an identical, but gramicidin-free solution. Recordings did not commence until the access resistance (*R*_a) had stabilized. If perforated-

patch configuration ruptured, the reversal potential of *E*_{IPSCs} would be 0 mV.

In cell-attached recordings, to determine neuronal firing frequency at layer V of mPFC, the recording pipettes were filled with ACSF. The pipette resistances were 3–6 M Ω . Ten micromolars of carbachol or 12 μ M NMDA was applied to induce neuronal firing in the mPFC. A Picospritzer (Parker Hannifin Instrumentation, Cleveland, OH) was used to puff 100 μ M isoguvacine via a pipette (5 M Ω) positioned close to the patched neurons with 50 ms pulse duration and 10 psi pressure.

All recordings were made with an Axopatch 200B amplifier through a DigiData 1321A interface (Molecular Devices, CA). The excitability recorded in current-clamp mode and postsynaptic currents (excitatory and inhibitory) recorded in voltage-clamp mode were analyzed with Clampfit 11.1. For the excitability experiments, number of action potential spikes per second was calculated. Reversal potentials were determined by measuring the shift of GABA_A-mediated inhibitory postsynaptic currents of pyramidal neurons patched at different holding potentials. The typical traces of miniature EPSCs or miniature IPSCs were selected to create a sample template for event detection within a data period, respectively. The frequency (event number) and amplitude of individual event was examined. The input resistances of the tested neurons were calculated offline from the voltage produced by negative current injection (-10 pA) prior to the step currents.

Stereotaxic injection of AAV

Mice were anesthetized with Avertin (200 mg/kg), and then were settled in a brain stereotaxic apparatus (RWD Life Science Co., Shenzhen, China). AAV2/Retro-hSyn-DIO-hM4D(Gi)-mCherry (1.43 \times 10¹³ v.g./ml), AAV2/Retro-hSyn-DIO-mCherry (1.43 \times 10¹³ v.g./ml), AAV2/9-Efla-DIO-eNpHR3.0-mCherry (1.43 \times 10¹³ v.g./ml), AAV2/9-Efla-DIO-mCherry (5.47 \times 10¹² v.g./ml), AAV2/9-hSyn-DIO-hM4D(Gi)-mCherry (8.66 \times 10¹² v.g./ml), AAV2/9-hSyn-DIO-mCherry (1.32 \times 10¹³ v.g./ml), AAV2/9-ChAT-mini TK promoter-*Ngfr*-3xFlag (2.54 \times 10¹² v.g./ml), AAV2/9-ChAT-mini TK promoter-3xFlag (1.2 \times 10¹² v.g./ml), AAV2/9-ChAT-mini TK promoter-EGFP-miR30shRNA(*Ngfr*) (5.13 \times 10¹² v.g./ml, CCGATGCTCCTATGGCTACTA), AAV2/9-ChAT-mini TK promoter-EGFP-miR30shRNA(NC) (5.92 \times 10¹² v.g./ml) were from OBiO Technology Corp. AAV2/9-hsyn-ACh3.0 (3.01 \times 10¹³ v.g./ml) was from WZ Biosciences Inc. For AAV injection, 300 nl AAV was administered bilaterally into the mPFC, HP, SI/nBM, and MS/vDB of ChAT-Cre mice, respectively, according to the experimental design. Ten milliliters of Hamilton syringe with a 33-gauge needle was used. The following coordinates defined brain area location, *mPFC*: anteroposterior, 1.94 mm; mediolateral, \pm 0.3 mm; and dorsoventral, -3.0 mm relative to the Bregma; *HP*: anteroposterior, -1.82 mm; mediolateral, \pm 1.3 mm; and dorsoventral, -1.5 mm relative to the Bregma; *SI/nBM*: anteroposterior, -0.6 mm; mediolateral, \pm 1.7 mm; and dorsoventral, -4.7 mm relative to the Bregma; *MS/vDB*: anteroposterior, 0.98 mm; mediolateral, \pm 0.3 mm; and dorsoventral, -5.0 mm relative to the Bregma. At the end of the infusion, the needle was kept in the brain for another 5 min to reduce backflow. Shortly after surgery, mice received Metacam (1mg/kg) for analgesia and were translocated to their home cages.

Immunofluorescence

Anesthetized mice were transcardially perfused with 50 mL of 4% paraformaldehyde in phosphate-buffered saline (PBS). Brains were removed and postfixed overnight at 4 °C. Twenty percent sucrose and 30% sucrose in PBS were sequentially used for cryopreservation. Brains were coronal sliced (30 μ m) by Leica CM1950. Slices were permeabilized with PBS and 0.3% Triton X-100 for 30 min and blocked in 5% BSA in PBS for 1 h, and incubated in diluted primary antibody (ChAT, AB144P, Millipore, 1:100, RRID:AB_2079751; NGFR, ab52987, Abcam,

1:200, RRID:AB_881682; Flag, 8146, CST, 1:500, RRID:AB_10950495) at 4 °C overnight. After incubation of secondary antibodies (Invitrogen Alex Fluor) at room temperature for 50 min and staining with 0.5 µg/ml DAPI for 5 min, coverslips were mounted and visualized with Olympos VS 120.

Immunoblotting

For western blot, mice brain tissues were lysed in RIPA buffer containing (all units are in mM): 50 Tris-HCl (pH 7.4), 150 NaCl, 2 EDTA, 1% NP-40, 0.5% sodium deoxycholate, 0.1% SDS, 100 PMSF, a cocktail of protease inhibitor (Roche), and phosphatase inhibitor (10 NaF, 1 Na₃VO₄). Supernatants obtained after centrifugation at 12,000 × *g* for 15 min at 4 °C were subjected to SDS-PAGE, and immunoblot analysis was performed with appropriate antibodies (KCC2, 07-432, Millipore, 1:1000, RRID:AB_310611; NKCC1, T4, Development Studies Hybridoma Bank, 1:200, RRID:AB_528406). Second antibodies were conjugated to infrared dyes (Rockland Immunochemicals, 1:1000). We detected bound antibody using Odyssey Infrared Imaging System and measured signal intensities with the image analysis software Odyssey. Samples were quantified and normalized as the ratio of target protein to control protein Tubulin. For the comparison between different genotypes or treatments, we presented the data as the fold change of one group to the other group.

Fiber photometry recording

For fiber photometry recording of ACh signals in the mPFC, mice were injected with AAV2/9-hsyn-ACh3.0 (WZ Biosciences Inc.) and implanted with an optic fiber (N.A. = 0.22) in the mPFC. Four weeks after viral expression, ACh signals were recorded by a commercial fiber photometry setup (Thinker Tech Nanjing Biotech Co. Ltd.). A 390-Hz sinusoidal blue LED light (480 nm) was used to excite ACh3.0, and the emission light was transformed into electronic waves by a PMT. The signal was low pass filtered with a cut-off frequency of 5 Hz. The laser intensity at the fiber tip was adjusted to 30–40 µW to minimize fluorescence bleaching. The recorded data were analyzed by MATLAB 2018b. We analyzed the recording data in a time window of 8 s, including 4 s before (−4 s to 0 s) and 4 s after (0 s to 4 s) object exploration. To detect the changes in ACh release for each object in the sample phase or the test phase, we calculate $\Delta F/F_0$ for the specific object separately. The values of signal $\Delta F/F_0$ were calculated with the following formula: $(F - F_0)/F_0$, where *F* represented the fluorescence signal and *F*₀ represented the averaged value of the signal for 10 s before the analysis.

Chemogenetics and optogenetics

For chemogenetic experiments, 300 nl AAV2/Retro-DIO-hM4D(Gi)-mCherry, AAV2/Retro-DIO-mCherry, or AAV2/9-hSyn-DIO-hM4D(Gi)-mCherry and AAV2/9-hSyn-DIO-mCherry (OBiO Technology Corp.) were bilaterally injected into the mPFC, HP or MS/vDB of ChAT-Cre mice. After 4 weeks of recovery period, behavioral tests were performed. Mice were injected with 1 mg/kg CNO (s.c., 1 mg/ml in 0.9% saline), 1 hour before behavioral tests.

For optogenetic experiments, AAV2/9-Ef1a-DIO-eNpHR3.0-mCherry or AAV2/9-Ef1a-DIO-mCherry (OBiO Technology Corp.) were bilaterally injected into the SI/nBM of ChAT-Cre mice and implanted with optical fiber in the mPFC. During temporal order recognition test, constant light with 589 nm was given to the cholinergic terminals in mPFC at 4–6 mW during the 5 min exploration in each phase.

Nicotine treatment

For chronic nicotine treatment, mice were given a drinking solution containing nicotine plus 1% saccharin to mask nicotine's bitter taste. Nicotine in the drinking water was applied at the dose of 650 µg/ml over a 4-week period. In order to apply sufficient nicotine, only nicotine-laced water will be administered to animals.

Cannula infusion of drug

For the bilateral cannula implantation into the mPFC of wild-type mice, the following coordinates were used: anteroposterior, 1.7 mm; mediolateral, ±1.5 mm (implantation with an angle of 20°); and dorsoventral, −2.75 mm relative to the Bregma. One week after the cannula implantation, behavioral experiments were performed. Furosemide was infused through cannula 1 h before the onset of novel object recognition and object location recognition tests. For the temporal order recognition test, furosemide was infused twice at the following time point, 1 h before the sample phase 1 and 1 h before the test phase. Specifically, furosemide sodium (2 mM) in a total volume of 500 nl per side was infused through an injector cannula with a microinfusion pump at a speed of 500 nl/min. The injection infuser was kept in the mPFC for 1 min after infusion.

Drugs

TTX, CNQX, APV, carbachol, picrotoxin, gramicidin, and nicotine bitartrate were from Sigma-Aldrich. Isoguvacine was purchased from Tocris Bioscience. Furosemide sodium was from Selleck.

Data analysis

Prism GraphPad 8.2.1 was used for statistical analysis. The statistical significance of differences between groups was calculated with unpaired two-sided *t*-test, two-way ANOVA with Bonferroni's or Sidak's multiple comparisons, and two-sided Wilcoxon rank-sum test, *p* value adjusted by FDR. Numerical data are means ± SEM. **p* < 0.05; ***p* < 0.01; ****p* < 0.001; *****p* < 0.0001; ns, not significant.

Reporting summary

Further information on research design is available in the Nature Portfolio Reporting Summary linked to this article.

Data availability

Data supporting the findings of this study are available within the main text and Supplementary Materials. Source data are provided with this paper as a Source Data file. All data are available from the corresponding author upon request. Source data are provided with this paper.

Code availability

Previously published and open-access software was used following the instructions. Descriptions are available in the “Methods” section.

References

1. Brown, M. W. & Aggleton, J. P. Recognition memory: what are the roles of the perirhinal cortex and hippocampus? *Nat. Rev. Neurosci.* **2**, 51–61 (2001).
2. Warburton, E. C. & Brown, M. W. Neural circuitry for rat recognition memory. *Behav. Brain Res.* **285**, 131–139 (2015).
3. Barker, G. R., Bird, F., Alexander, V. & Warburton, E. C. Recognition memory for objects, place, and temporal order: a disconnection analysis of the role of the medial prefrontal cortex and perirhinal cortex. *J. Neurosci.* **27**, 2948–2957 (2007).
4. Warburton, E. C. & Brown, M. W. Findings from animals concerning when interactions between perirhinal cortex, hippocampus and medial prefrontal cortex are necessary for recognition memory. *Neuropsychologia* **48**, 2262–2272 (2010).
5. Morici, J. F., Bekinschtein, P. & Weisstaub, N. V. Medial prefrontal cortex role in recognition memory in rodents. *Behav. Brain Res.* **292**, 241–251 (2015).
6. Barker, G. R. & Warburton, E. C. Critical role of the cholinergic system for object-in-place associative recognition memory. *Learn. Mem.* **16**, 8–11 (2009).
7. Boess, F. G. et al. The novel alpha7 nicotinic acetylcholine receptor agonist N-[(3R)-1-azabicyclo[2.2.2]oct-3-yl]-7-[2-(methoxy)phenyl]

- 1-benzofuran-2-carboxamide improves working and recognition memory in rodents. *J. Pharmacol. Exp. Ther.* **321**, 716–725 (2007).
8. De Jaeger, X. et al. Decreased acetylcholine release delays the consolidation of object recognition memory. *Behav. Brain Res.* **238**, 62–68 (2013).
 9. Melichercik, A. M., Elliott, K. S., Bianchi, C., Ernst, S. M. & Winters, B. D. Nicotinic receptor activation in perirhinal cortex and hippocampus enhances object memory in rats. *Neuropharmacology* **62**, 2096–2105 (2012).
 10. Winters, B. D., Bartko, S. J., Saksida, L. M. & Bussey, T. J. Scopopolamine infused into perirhinal cortex improves object recognition memory by blocking the acquisition of interfering object information. *Learn. Mem.* **14**, 590–596 (2007).
 11. Ananth, M. R., Rajebhosale, P., Kim, R., Talmage, D. A. & Role, L. W. Basal forebrain cholinergic signalling: development, connectivity and roles in cognition. *Nat. Rev. Neurosci.* **24**, 233–251 (2023).
 12. Wu, Z., Lin, D. & Li, Y. Pushing the frontiers: tools for monitoring neurotransmitters and neuromodulators. *Nat. Rev. Neurosci.* **23**, 257–274 (2022).
 13. Ballinger, E. C., Ananth, M., Talmage, D. A. & Role, L. W. Basal forebrain cholinergic circuits and signaling in cognition and cognitive decline. *Neuron* **91**, 1199–1218 (2016).
 14. Semba, K. & Fibiger, H. C. Time of origin of cholinergic neurons in the rat basal forebrain. *J. Comp. Neurol.* **269**, 87–95 (1988).
 15. Zaborszky, L. et al. Specific basal forebrain-cortical cholinergic circuits coordinate cognitive operations. *J. Neurosci.* **38**, 9446–9458 (2018).
 16. Boskovic, Z. et al. Regulation of cholinergic basal forebrain development, connectivity, and function by neurotrophin receptors. *Neuronal Signal.* **3**, NS20180066 (2019).
 17. Yang, F. et al. Pro-BDNF-induced synaptic depression and retraction at developing neuromuscular synapses. *J. Cell Biol.* **185**, 727–741 (2009).
 18. Koshimizu, H. et al. Multiple functions of precursor BDNF to CNS neurons: negative regulation of neurite growth, spine formation and cell survival. *Mol. Brain* **2**, 1756–6606 (2009).
 19. Sun, Y. et al. ProBDNF collapses neurite outgrowth of primary neurons by activating RhoA. *PLoS ONE* **7**, e35883 (2012).
 20. Je, H. S. et al. Role of pro-brain-derived neurotrophic factor (proBDNF) to mature BDNF conversion in activity-dependent competition at developing neuromuscular synapses. *Proc. Natl Acad. Sci. USA* **109**, 15924–15929 (2012).
 21. Hefti, F., Hartikka, J., Salvatierra, A., Weiner, W. J. & Mash, D. C. Localization of nerve growth factor receptors in cholinergic neurons of the human basal forebrain. *Neurosci. Lett.* **69**, 37–41 (1986).
 22. Roux, P. P. & Barker, P. A. Neurotrophin signaling through the p75 neurotrophin receptor. *Prog. Neurobiol.* **67**, 203–233 (2002).
 23. Springer, J. E., Koh, S., Tayrien, M. W. & Loy, R. Basal forebrain magnocellular neurons stain for nerve growth factor receptor: correlation with cholinergic cell bodies and effects of axotomy. *J. Neurosci. Res.* **17**, 111–118 (1987).
 24. Peterson, D. A., Dickinson-Anson, H. A., Leppert, J. T., Lee, K. F. & Gage, F. H. Central neuronal loss and behavioral impairment in mice lacking neurotrophin receptor p75. *J. Comp. Neurol.* **404**, 1–20 (1999).
 25. Peterson, D. A., Leppert, J. T., Lee, K. F. & Gage, F. H. Basal forebrain neuronal loss in mice lacking neurotrophin receptor p75. *Science* **277**, 837 (1997).
 26. Greferath, U. et al. Enlarged cholinergic forebrain neurons and improved spatial learning in p75 knockout mice. *Eur. J. Neurosci.* **12**, 885–893 (2000).
 27. Ward, N. L. & Hagg, T. p75(NGFR) and cholinergic neurons in the developing forebrain: a re-examination. *Brain Res. Dev. Brain Res.* **118**, 79–91 (1999).
 28. Yeo, T. T. et al. Absence of p75NTR causes increased basal forebrain cholinergic neuron size, choline acetyltransferase activity, and target innervation. *J. Neurosci.* **17**, 7594–7605 (1997).
 29. Naumann, T. et al. Complete deletion of the neurotrophin receptor p75NTR leads to long-lasting increases in the number of basal forebrain cholinergic neurons. *J. Neurosci.* **22**, 2409–2418 (2002).
 30. Boskovic, Z. et al. The role of p75NTR in cholinergic basal forebrain structure and function. *J. Neurosci.* **34**, 13033–13038 (2014).
 31. Boskovic, Z. et al. Cholinergic basal forebrain neurons regulate fear extinction consolidation through p75 neurotrophin receptor signaling. *Transl. Psychiatry* **8**, 199 (2018).
 32. Meier, S. et al. The p75 neurotrophin receptor is required for the survival of neuronal progenitors and normal formation of the basal forebrain, striatum, thalamus and neocortex. *Development* **146**, dev181933 (2019).
 33. Ren, J. et al. Habenula “cholinergic” neurons co-release glutamate and acetylcholine and activate postsynaptic neurons via distinct transmission modes. *Neuron* **69**, 445–452 (2011).
 34. Saunders, A. et al. Molecular diversity and specializations among the cells of the adult mouse brain. *Cell* **174**, 1015–1030.e1016 (2018).
 35. Zeisel, A. et al. Molecular architecture of the mouse nervous system. *Cell* **174**, 999–1014.e1022 (2018).
 36. Winters, B. D. & Bussey, T. J. Removal of cholinergic input to perirhinal cortex disrupts object recognition but not spatial working memory in the rat. *Eur. J. Neurosci.* **21**, 2263–2270 (2005).
 37. Devito, L. M. & Eichenbaum, H. Memory for the order of events in specific sequences: contributions of the hippocampus and medial prefrontal cortex. *J. Neurosci.* **31**, 3169–3175 (2011).
 38. Chiba, A. A., Kesner, R. P. & Gibson, C. J. Memory for temporal order of new and familiar spatial location sequences: role of the medial prefrontal cortex. *Learn. Mem.* **4**, 311–317 (1997).
 39. Jing, M. et al. A genetically encoded fluorescent acetylcholine indicator for in vitro and in vivo studies. *Nat. Biotechnol.* **36**, 726–737 (2018).
 40. Jing, M. et al. An optimized acetylcholine sensor for monitoring in vivo cholinergic activity. *Nat. Methods* **17**, 1139–1146 (2020).
 41. Picciotto, M. R., Higley, M. J. & Mineur, Y. S. Acetylcholine as a neuromodulator: cholinergic signaling shapes nervous system function and behavior. *Neuron* **76**, 116–129 (2012).
 42. Liu, Z., Neff, R. A. & Berg, D. K. Sequential interplay of nicotinic and GABAergic signaling guides neuronal development. *Science* **314**, 1610–1613 (2006).
 43. Ebihara, S., Shirato, K., Harata, N. & Akaike, N. Gramicidin-perforated patch recording: GABA response in mammalian neurons with intact intracellular chloride. *J. Physiol.* **484**, 77–86 (1995).
 44. Deidda, G. et al. Reversing excitatory GABAAR signaling restores synaptic plasticity and memory in a mouse model of Down syndrome. *Nat. Med.* **21**, 318–326 (2015).
 45. Simonnet, C. et al. Silencing KCC2 in mouse dorsal hippocampus compromises spatial and contextual memory. *Neuropsychopharmacology* **48**, 1067–1077 (2023).
 46. Kahle, K. T. et al. Roles of the cation-chloride cotransporters in neurological disease. *Nat. Clin. Pract. Neurol.* **4**, 490–503 (2008).
 47. Kaila, K., Price, T. J., Payne, J. A., Puskarjov, M. & Voipio, J. Cation-chloride cotransporters in neuronal development, plasticity and disease. *Nat. Rev. Neurosci.* **15**, 637–654 (2014).
 48. Blaesse, P., Airaksinen, M. S., Rivera, C. & Kaila, K. Cation-chloride cotransporters and neuronal function. *Neuron* **61**, 820–838 (2009).
 49. Kruse, A. C. et al. Muscarinic acetylcholine receptors: novel opportunities for drug development. *Nat. Rev. Drug Discov.* **13**, 549–560 (2014).
 50. Taly, A., Corringer, P. J., Guedin, D., Lestage, P. & Changeux, J. P. Nicotinic receptors: allosteric transitions and therapeutic targets in the nervous system. *Nat. Rev. Drug Discov.* **8**, 733–750 (2009).

51. Le Houezec, J. Role of nicotine pharmacokinetics in nicotine addiction and nicotine replacement therapy: a review. *Int. J. Tuberc. Lung Dis.* **7**, 811–819 (2003).
52. Uva, L. et al. Acute induction of epileptiform discharges by pilocarpine in the in vitro isolated guinea-pig brain requires enhancement of blood-brain barrier permeability. *Neuroscience* **151**, 303–312 (2008).
53. Satta, R. et al. Nicotine decreases DNA methyltransferase 1 expression and glutamic acid decarboxylase 67 promoter methylation in GABAergic interneurons. *Proc. Natl Acad. Sci. USA* **105**, 16356–16361 (2008).
54. Ibanez, C. F. & Simi, A. p75 neurotrophin receptor signaling in nervous system injury and degeneration: paradox and opportunity. *Trends Neurosci.* **35**, 431–440 (2012).
55. Dechant, G. & Barde, Y. A. The neurotrophin receptor p75(NTR): novel functions and implications for diseases of the nervous system. *Nat. Neurosci.* **5**, 1131–1136 (2002).
56. Hempstead, B. L. The many faces of p75NTR. *Curr. Opin. Neurobiol.* **12**, 260–267 (2002).
57. Woo, N. H. et al. Activation of p75NTR by proBDNF facilitates hippocampal long-term depression. *Nat. Neurosci.* **8**, 1069–1077 (2005).
58. Lu, B., Pang, P. T. & Woo, N. H. The yin and yang of neurotrophin action. *Nat. Rev. Neurosci.* **6**, 603–614 (2005).
59. Peterson, D. A., Leppert, J. T., Lee, K. F. & Gage, F. H. Basal forebrain neuronal loss in mice lacking neurotrophin receptor p75. *Science* **277**, 837–839 (1997).
60. Luther, J. A. & Birren, S. J. p75 and TrkA signaling regulates sympathetic neuronal firing patterns via differential modulation of voltage-gated currents. *J. Neurosci.* **29**, 5411–5424 (2009).
61. Zhang, Y. H., Chi, X. X. & Nicol, G. D. Brain-derived neurotrophic factor enhances the excitability of rat sensory neurons through activation of the p75 neurotrophin receptor and the sphingomyelin pathway. *J. Physiol.* **586**, 3113–3127 (2008).
62. Zhu, F., Elnozahy, S., Lawlor, J. & Kuchibhotla, K. V. The cholinergic basal forebrain provides a parallel channel for state-dependent sensory signaling to auditory cortex. *Nat. Neurosci.* **26**, 810–819 (2023).
63. Lohani, S. et al. Spatiotemporally heterogeneous coordination of cholinergic and neocortical activity. *Nat. Neurosci.* **25**, 1706–1713 (2022).
64. Parikh, V., Kozak, R., Martinez, V. & Sarter, M. Prefrontal acetylcholine release controls cue detection on multiple timescales. *Neuron* **56**, 141–154 (2007).
65. Gill, T. M., Sarter, M. & Givens, B. Sustained visual attention performance-associated prefrontal neuronal activity: evidence for cholinergic modulation. *J. Neurosci.* **20**, 4745–4757 (2000).
66. Pancani, T. et al. Cholinergic deficits selectively boost cortical intratelencephalic control of striatum in male Huntington’s disease model mice. *Nat. Commun.* **14**, 1398 (2023).
67. Oswald, M. J. et al. Cholinergic basal forebrain nucleus of Meynert regulates chronic pain-like behavior via modulation of the prelimbic cortex. *Nat. Commun.* **13**, 5014 (2022).
68. Li, X. et al. Generation of a whole-brain atlas for the cholinergic system and mesoscopic projectome analysis of basal forebrain cholinergic neurons. *Proc. Natl Acad. Sci. USA* **115**, 415–420 (2018).
69. Descarries, L., Gisiger, V. & Steriade, M. Diffuse transmission by acetylcholine in the CNS. *Prog. Neurobiol.* **53**, 603–625 (1997).
70. Gritton, H. J. et al. Cortical cholinergic signaling controls the detection of cues. *Proc. Natl Acad. Sci. USA* **113**, E1089–E1097 (2016).
71. Parikh, V. et al. Rapid assessment of in vivo cholinergic transmission by amperometric detection of changes in extracellular choline levels. *Eur. J. Neurosci.* **20**, 1545–1554 (2004).
72. Sarter, M., Lustig, C., Howe, W. M., Gritton, H. & Berry, A. S. Deterministic functions of cortical acetylcholine. *Eur. J. Neurosci.* **39**, 1912–1920 (2014).
73. Cabeza, R. & Nyberg, L. Imaging cognition II: an empirical review of 275 PET and fMRI studies. *J. Cogn. Neurosci.* **12**, 1–47 (2000).
74. Kahn, I., Davachi, L. & Wagner, A. D. Functional-neuroanatomic correlates of recollection: implications for models of recognition memory. *J. Neurosci. Off. J. Soc. Neurosci.* **24**, 4172–4180 (2004).
75. Kessels, R. P., Postma, A., Wijnalda, E. M. & de Haan, E. H. Frontal-lobe involvement in spatial memory: evidence from PET, fMRI, and lesion studies. *Neuropsychol. Rev.* **10**, 101–113 (2000).
76. Meunier, M., Bachevalier, J. & Mishkin, M. Effects of orbital frontal and anterior cingulate lesions on object and spatial memory in rhesus monkeys. *Neuropsychologia* **35**, 999–1015 (1997).
77. Bachevalier, J. & Mishkin, M. Visual recognition impairment follows ventromedial but not dorsolateral prefrontal lesions in monkeys. *Behav. Brain Res.* **20**, 249–261 (1986).
78. Barker, G. R. & Warburton, E. C. When is the hippocampus involved in recognition memory? *J. Neurosci. Off. J. Soc. Neurosci.* **31**, 10721–10731 (2011).
79. He, C. Y. et al. Association of rs2072446 in the NGFR gene with the risk of Alzheimer’s disease and amyloid-beta deposition in the brain. *CNS Neurosci. Ther.* **28**, 2218–2229 (2022).
80. Ripke, S. et al. Genome-wide association analysis identifies 13 new risk loci for schizophrenia. *Nat. Genet.* **45**, 1150–1159 (2013).
81. Zhao, L. et al. NGFR gene and single nucleotide polymorphisms, rs2072446 and rs11466162, playing roles in psychiatric disorders. *Brain Sci.* **12**, 1372 (2022).
82. Tang, X., Jaenisch, R. & Sur, M. The role of GABAergic signalling in neurodevelopmental disorders. *Nat. Rev. Neurosci.* **22**, 290–307 (2021).
83. Rivera, C. et al. The K⁺/Cl⁻ co-transporter KCC2 renders GABA hyperpolarizing during neuronal maturation. *Nature* **397**, 251–255 (1999).
84. Bortone, D. & Polleux, F. KCC2 expression promotes the termination of cortical interneuron migration in a voltage-sensitive calcium-dependent manner. *Neuron* **62**, 53–71 (2009).
85. Hinz, L., Torrella Barrufet, J. & Heine, V. M. KCC2 expression levels are reduced in post mortem brain tissue of Rett syndrome patients. *Acta Neuropathol. Commun.* **7**, 196 (2019).
86. Talos, D. M. et al. Altered inhibition in tuberous sclerosis and type IIb cortical dysplasia. *Ann. Neurol.* **71**, 539–551 (2012).
87. Merner, N. D. et al. Regulatory domain or CpG site variation in SLC12A5, encoding the chloride transporter KCC2, in human autism and schizophrenia. *Front. Cell. Neurosci.* **9**, 386 (2015).
88. Magno, L. et al. Fate mapping reveals mixed embryonic origin and unique developmental codes of mouse forebrain septal neurons. *Commun. Biol.* **5**, 1137 (2022).
89. Gielow, M. R. & Zaborszky, L. The input-output relationship of the cholinergic basal forebrain. *Cell Rep.* **18**, 1817–1830 (2017).
90. Nilbratt, M., Porras, O., Marutle, A., Hovatta, O. & Nordberg, A. Neurotrophic factors promote cholinergic differentiation in human embryonic stem cell-derived neurons. *J. Cell. Mol. Med.* **14**, 1476–1484 (2010).
91. Unal, C. T., Golowasch, J. P. & Zaborszky, L. Adult mouse basal forebrain harbors two distinct cholinergic populations defined by their electrophysiology. *Front. Behav. Neurosci.* **6**, 21 (2012).
92. Laszlovszky, T. et al. Distinct synchronization, cortical coupling and behavioral function of two basal forebrain cholinergic neuron types. *Nat. Neurosci.* **23**, 992–1003 (2020).
93. Lee, K. F. et al. Targeted mutation of the gene encoding the low affinity NGF receptor p75 leads to deficits in the peripheral sensory nervous system. *Cell* **69**, 737–749 (1992).
94. Gong, S. et al. A gene expression atlas of the central nervous system based on bacterial artificial chromosomes. *Nature* **425**, 917–925 (2003).
95. Hao, Y. et al. Integrated analysis of multimodal single-cell data. *Cell* **184**, 3573–3587.e3529 (2021).

96. Wu, T. et al. clusterProfiler 4.0: A universal enrichment tool for interpreting omics data. *Innovation* **2**, 100141 (2021).

Acknowledgements

This work was supported by the National Key Research and Development Program of China (2017YFE0126500), the National Natural Science Foundation of China (31730034, U22A20299), Beijing Advanced Innovation Center for Human Brain Protection, Beijing Academy of Artificial Intelligence (BAAI, 20222001736) to B.L., Beijing Municipal Natural Science Foundation (L222077 and IS23097) to F.Y., and National Natural Science Foundation of China (82071207, 81200829), Beijing Municipal Natural Science Foundation (7232099) to F.M. Selected artwork shown in working model were used from or adapted from pictures provided by Servier Medical Art, licensed under a Creative Commons Attribution 4.0 unported license (<https://creativecommons.org/licenses/by/4.0>).

Author contributions

B.L., F.Y., and F.M. conceived the study and designed the major experiments. F.M., C.Z., S.L. Z.X., Y.Z., Y.X., R.Y., H.Y., X.H., G.C., and F.Y. performed the experiments. P.Y. analyzed the single-cell RNA sequencing data. B.L., F.Y., and D.W. supervised the study. The manuscript was written by F.M., F.Y., and B.L. with input from all of the authors.

Competing interests

The authors declare no competing interests.

Additional information

Supplementary information The online version contains supplementary material available at <https://doi.org/10.1038/s41467-024-51707-w>.

Correspondence and requests for materials should be addressed to Feng Yang or Bai Lu.

Peer review information *Nature Communications* thanks Haohong Li, Kazuto Kobayashi, and the other anonymous reviewer for their contribution to the peer review of this work. A peer review file is available.

Reprints and permissions information is available at <http://www.nature.com/reprints>

Publisher's note Springer Nature remains neutral with regard to jurisdictional claims in published maps and institutional affiliations.

Open Access This article is licensed under a Creative Commons Attribution-NonCommercial-NoDerivatives 4.0 International License, which permits any non-commercial use, sharing, distribution and reproduction in any medium or format, as long as you give appropriate credit to the original author(s) and the source, provide a link to the Creative Commons licence, and indicate if you modified the licensed material. You do not have permission under this licence to share adapted material derived from this article or parts of it. The images or other third party material in this article are included in the article's Creative Commons licence, unless indicated otherwise in a credit line to the material. If material is not included in the article's Creative Commons licence and your intended use is not permitted by statutory regulation or exceeds the permitted use, you will need to obtain permission directly from the copyright holder. To view a copy of this licence, visit <http://creativecommons.org/licenses/by-nc-nd/4.0/>.

© The Author(s) 2024

¹Institute of Systems Biomedicine, School of Basic Medical Sciences, Peking University Health Science Center, Beijing, China. ²School of Pharmaceutical Sciences, IDG/McGovern Institute for Brain Research, Tsinghua University, Beijing, China. ³Basic and Translational Medicine Center, China National Clinical Research Center for Neurological Diseases, Beijing Tiantan Hospital, Capital Medical University, Beijing, China. ⁴Advanced Innovation Center for Human Brain Protection, Capital Medical University, Beijing, China. ⁵School of Basic Medicine, Capital Medical University, Beijing, China. ⁶Laboratory of Cognitive and Behavioral Disorders, Beijing Institute of Brain Disorders, Capital Medical University, Beijing, China. ⁷Department of Pharmacology and Molecular Sciences, Lieber Institute for Brain Development, Johns Hopkins University School of Medicine, Baltimore, MD, USA.

✉ e-mail: fengyang@cmmu.edu.cn; bai_lu@tsinghua.edu.cn